



**UNIVERSITE PARIS-SUD XI**  
**Faculté des Sciences d'Orsay**



**THÈSE DE DOCTORAT**

**SPECIALITE : PHYSIQUE**

*Ecole Doctorale « Sciences et Technologies de l'Information des  
Télécommunications et des Systèmes »*

Présentée par :

**Ali Khaleghi**

Sujet :

**Diversity Antennas for Wireless LAN and Mobile  
Communication Handsets**

**« Etude d'antennes en Diversité pour Téléphone Mobiles et Réseaux  
Locaux Radio électriques »**

Soutenance le 18 Septembre 2006 devant le jury composé de :

M. A. Azoulay	Professeur à Supélec de Gif-sur-Yvette	Examineur
M. J-C. Bolomey	Professeur à l'Université Paris XI	Directeur de thèse
M. P. Degauque	Professeur à l'Université de Lille 1	Président
M. M. Drissi	Professeur à l'Université de Rennes	Rapporteur
M. P-S. Kildal	Professeur à Chalmers University of Technology	Rapporteur



# **Etude d'Antennes en Diversité pour Téléphones Mobiles et Réseaux Locaux Radioélectriques**

**Khaleghi, A.**

## **Résumé**

Des niveaux élevés du rapport signal/bruit (SNR) sont nécessaires pour obtenir une bonne qualité de service et de hauts débits pour les nouvelles générations de téléphones mobiles (3G, 3,5 G) et pour les réseaux locaux sans fil (WiFi IEEE 802.11b/g/a). Afin d'améliorer le SNR et de faire face aux effets de l'environnement (trajets multiples, diffraction, brouillages) sur la transmission de données, il est possible d'appliquer aux systèmes de radiocommunications, des techniques de diversité.

Cette thèse vise à approfondir les techniques de diversité appliquées aux mobiles de radiotéléphonie et aux modules de réseaux locaux radioélectriques et à montrer les possibilités d'amélioration de ces techniques en incluant plusieurs antennes dans le système.

L'amélioration apportée par la diversité va dépendre très fortement des caractéristiques des antennes utilisées et de l'environnement électromagnétique. Au préalable, il est nécessaire de caractériser la propagation mobile : pour cela, différents canaux mobiles de propagation sont étudiés et un simulateur de fading (trajets multiples) est développé. Le simulateur de fading est combiné à une modélisation des angles d'arrivée (AoA) afin de pouvoir calculer les performances des terminaux radio incorporant de multiples antennes. La vérification de l'approche théorique est effectuée grâce à des mesures réalisées dans la chambre réverbérante de Supelec. De plus, les caractéristiques statistiques des signaux dus aux trajets multiples dans la chambre réverbérante sont étudiées en détail.

En utilisant les méthodes proposées, les améliorations apportées par les techniques de diversité d'antenne sont étudiés, en mettant l'accent sur le gain de diversité.

La diversité d'antenne est étudiée dans un premier temps, pour deux antennes dipôles parallèles en fonction de la distance de séparation de ces antennes, et validée ensuite par les simulations et les mesures conduites dans la chambre réverbérante de Supelec. La diversité de phase et du diagramme de rayonnement est identifiée et calculée pour des antennes proches.

En fonction de ces résultats, un système simple et compact de diversité d'antenne de téléphone mobile est réalisé. Ses performances prenant en compte le modèle humain de fantôme (SAM) sont analysées à travers, entre autres, deux paramètres fondamentaux dans ce type d'étude : le coefficient de corrélation des signaux incidents et le gain efficace moyen de diversité (MEG).

Finalement, quatre systèmes compacts différents de diversité d'antenne ont été conçus, simulés et réalisés pour des applications de réseaux locaux sans fil (WLAN). Les antennes considérées ici utilisent la diversité de polarisation, de diagramme de rayonnement et de phase en vue de l'amélioration de la qualité de réception du signal en présence de trajets multiples. L'efficacité de la diversité est vérifiée par des simulations électromagnétiques et par des mesures.

# **Diversity Antennas for Wireless LAN and Mobile Communication Handsets**

Khaleghi, A.

## **Abstract**

High signal to noise ratio (SNR) levels are required to provide high data rate transmission for the next generation of mobile and wireless devices. In order to provide high SNR and to cope with the environmental impacts on the data transmission, diversity techniques are used. This thesis investigates the performance enhancement that can be delivered by including more antennas in the system.

The performance enhancement is dependent on the characteristics of the antennas and on the wave propagation environment. Different mobile propagation channels are investigated and a fading simulator is improved. The fading simulator is combined with the spherical models for the field angle of arrivals to be able to calculate the performance of wireless terminals with multiple antennas. The verification of the computations is performed by measurements conducted in Supelec reverberation chamber. Furthermore, the statistical characteristics of the multipath fading signals in the reverberation chamber are investigated in detail.

Using the proposed methods, the antenna diversity performance enhancements in relation to the relative displacement and orientation of the antennas and various spherical field models are studied. Furthermore the gain improvements for the channels with correlated signals and unbalanced powers are investigated.

Antenna diversity is studied for two parallel dipole antennas in relation to the separation distance by the simulations and measurements in reverberation chamber. Radiation pattern phase diversity is depicted for the coupled antennas. A simple and compact mobile phone antenna diversity system is developed and the performance including phantom human head model is investigated through mean effective gain, signals correlation coefficient and diversity gain.

## Abstract

Four different and compact antenna diversity systems are designed, simulated and manufactured for wireless LAN applications. The antennas make use of polarization, pattern and phase diversities for signals reception in multipath channels. The performance enhancement of the antenna systems are explored by the simulations and the measurements.

## Table of Contents

Chapter 1	Introduction .....	1
1.1	Objectives for this Thesis .....	2
1.2	Organization of the Thesis.....	4
Chapter 2	Multipath Fading Characterization.....	6
2.1	Introduction .....	6
2.2	Characterization of Mobile Radio Propagation.....	6
2.3	The Nature of Multipath Propagation.....	8
2.4	The Challenge of Communication over Fading Channels.....	9
2.5	Short-term Fading.....	11
2.6	Fading Models .....	12
2.6.1	Rayleigh fading model.....	14
2.6.2	Rician fading model .....	15
2.7	Fading Simulator .....	15
2.8	Fading Simulator Models .....	16
2.9	Empirical and Mathematical AoA Models.....	20
2.10	Cross Polarization Power Ratio (XPR) .....	28
2.11	Mean Effective Gain (MEG) .....	30
2.11.1	MEG measurements .....	32
2.12	Summary.....	34
Chapter 3	Fading Simulator, Field Simulator and Reverberation Chamber .....	36
3.1	Introduction .....	36
3.2	New Improved Fading Simulator .....	37
3.3	Field Simulator .....	42
3.4	New Improved Field Simulator .....	45
3.5	Random Field Measurements .....	47
3.6	Reverberation Chamber Enclosure.....	50
3.6.1	Test frequency range .....	52
3.6.2	Antennas .....	54
3.6.3	Working volume .....	54
3.6.4	Mode modification techniques .....	54
3.7	MSRC Excitation and Signal Acquisition.....	56
3.8	Statistical Characterization.....	61
3.9	Statistical Characteristics of Supelec MSRC .....	63
3.10	Cross Polarization Ratio .....	72
3.11	Field Periodicity Test .....	73
3.12	MEG and Antenna Efficiency Evaluation inside MSRC .....	75
3.13	Summary.....	76
Chapter 4	Multipath Fading Mitigation and Antenna Diversity .....	78
4.1	Introduction .....	78
4.2	Diversity Reception .....	79
4.3	Diversity Methods .....	80
4.3.1	Selection combining .....	82

## Table of Contents

4.3.2	Maximum ratio combining .....	84
4.3.3	Equal-gain combining .....	85
4.4	Improvements from Diversity .....	85
4.4.1	Level Crossing Rate and Average Fade Duration .....	90
4.5	Diversity and Signals Correlation Coefficient.....	92
4.5.1	Correlation coefficient: mutual impedance .....	93
4.5.2	Correlation coefficient: radiation pattern .....	94
4.5.3	Correlation coefficient: signals.....	95
4.6	Correlation Coefficient for Space Diversity Antennas: Pattern Approach.....	96
4.7	Correlation Coefficient for Space Diversity Antennas: Signal Analysis .....	100
4.8	Diversity Gain for Space Diversity Antennas: Signal Analysis.....	103
4.9	Diversity Gain for Correlated Signals: Numerical Results .....	106
4.10	Diversity Gain for Correlated Signals and Imbalance Branches.....	108
4.11	Diversity Evaluation from Measured Signals.....	110
4.12	Reverberation Chamber Measurements.....	111
4.12.1	Spatial correlation coefficient for reverberation chamber.....	111
4.12.2	LCR and AFD inside reverberation chamber.....	116
4.13	Summery.....	117
Chapter 5	Antenna Diversity for Mobile Phone Communication.....	119
5.1	Introduction .....	119
5.2	Diversity Techniques with Parallel Dipole Antennas: Pattern Analysis .....	120
5.2.1	Signals Correlation coefficient: radiation pattern.....	122
5.2.2	Measurement setup .....	129
5.2.3	Diversity gain .....	132
5.2.4	Antenna efficiency.....	134
5.2.5	Diversity gain versus separation distance: simulation.....	135
5.3	Antenna Diversity With Parasitic Elements .....	136
5.4	Compact and Dual Band Antenna Diversity for Mobile Phones .....	139
5.4.1	Antenna prototype .....	140
5.4.2	Antenna simulation and measurement.....	141
5.4.3	Farfield radiation pattern .....	143
5.4.4	Signals correlation coefficient: mutual impedance .....	146
5.4.5	Signals correlation coefficient for GSM band: pattern approach.....	146
5.4.6	Diversity gain using field simulator for GSM band .....	148
5.4.7	Antenna diversity performance for DCS band .....	151
5.4.8	Antenna diversity measurement for GSM and DCS bands .....	152
5.4.9	Antenna measurement using head model: GSM and DCS bands .....	155
5.4.10	Correlation coefficient and diversity techniques.....	158
5.4.11	Local correlation coefficient.....	159
5.5	Summery.....	161
Chapter 6	Polarization, Pattern and Phase Diversity Antennas for Wireless LAN Applications.....	163
6.1	Introduction .....	163
6.2	Polarization Diversity Antenna for WLANs .....	164
6.2.1	Antenna configuration and modeling .....	165

## Table of Contents

6.2.2	Theoretical Analysis .....	166
6.2.3	Antenna simulation and measurements .....	166
6.2.4	Radiation pattern.....	167
6.2.5	Antenna diversity evaluation .....	168
6.2.6	Far-field pattern analysis of circular patch polarization diversity antenna 171	
6.2.7	Conclusion .....	176
6.3	Pattern Diversity Antennas Using Parasitic Switching Elements .....	177
6.3.1	Preliminary research .....	179
6.3.2	Main radiator antenna design .....	182
6.3.3	Antenna simulation and measurement.....	186
6.3.4	Diversity performance simulation .....	188
6.3.5	Diversity performance measurement.....	190
6.3.6	Conclusion.....	191
6.4	Integrated Diversity Antenna for WLANs .....	191
6.4.1	Preliminary .....	192
6.4.2	Antenna design .....	193
6.4.3	Antenna simulation and optimization.....	194
6.4.4	Farfield radiation pattern .....	196
6.4.5	Diversity antenna parameters evaluation.....	198
6.4.6	Mean signal power .....	203
6.4.7	Radiation pattern analysis and diversity techniques.....	203
6.4.8	Conclusion.....	203
6.5	A Compact and Broadband Diversity Antenna for WLANs.....	204
6.5.1	Diversity antenna design .....	205
6.5.2	Return loss and coupling .....	206
6.5.3	Radiation pattern.....	207
6.5.4	Signals correlation coefficient.....	208
6.5.5	Signals measurement .....	209
6.5.6	Radiation pattern analysis and diversity techniques.....	211
6.5.7	Mean signal power .....	211
6.5.8	Conclusion.....	211
6.6	Diversity Gain Enhancement for WLAN antennas .....	212
6.7	Summary.....	213
	Conclusion.....	215
	References.....	218
	Appendix I .....	224
	Appendix II.....	226
	Appendix III.....	228

## List of Figures

Figure 2-1 Typical mobile radio scenario illustrating multipath propagation in a terrestrial mobile radio environment [1].....	7
Figure 2-2 Constructive and destructive addition of two transmission paths.....	8
Figure 2-3 How the envelope fades as two incoming signals combine with different phases 9	
Figure 2-4 Typical behavior of the received signal in mobile communications [3].....	9
Figure 2-5 Spatial frame of reference: $\varphi$ is in the horizontal plane ( $xy$ - plane); $\theta$ is in the vertical plane .....	12
Figure 2-6 PDF of the Rayleigh distribution.....	14
Figure 2-7 Comparison among autocorrelation of the simulated complex fading; Jakes model, improved Jakes model and Clarke reference model.....	18
Figure 2-8 Comparison among autocorrelation of the simulated real-part fading; Jakes model, improved Jakes model and Clarke reference model.....	19
Figure 2-9 Comparison among autocorrelation of the simulated imaginary-part fading; Jakes model, improved Jakes model and Clarke reference model .....	19
Figure 2-10 Comparison among cross-correlation of the simulated fading signals; Jakes model, improved Jakes model and Clarke reference model (note that the reference model is always zero).....	20
Figure 2-11 Spherical coordinate system and incident field representation.....	21
Figure 2-12 Form of the RF power spectrum using different scattering models: (—) Clarke’s model, (---) Aulin’s model, (- - -) improved Aulin model; $\theta_m=45^\circ$ [3] .....	22
Figure 2-13 Two truncated Gaussian functions corresponds to field elevation plane AoA distributions in urban environments .....	24
Figure 2-14 Illustration of the AoA distribution in various multipath propagation channels (a) <i>Clarke</i> model $M_1$ , uniform distribution in azimuth plane only (b) <i>Taga</i> model $M_2$ , Uniform distribution in azimuth and Gaussian distribution in the elevation (c) <i>Kalliola</i> model $M_3$ , Uniform azimuth and double exponential in elevation (d) <i>Knudsen</i> model $M_4$ , Gaussian distribution in elevation and elliptical distribution in azimuth; Red color show high dense scatters.....	28
Figure 2-15 Mean effective gain of evaluated antennas, PIFA, MEMO, Discone in different multipath scattering field environments [25] .....	32
Figure 2-16 Half wavelengths dipole antenna and its coordinate, $\alpha$ is the dipole inclination angle .....	33
Figure 2-17 MEG of inclined half wavelengths dipole antenna in an environment with Gaussian distribution in elevation plane ( $m_v=m_H=0^\circ$ and $\sigma_v=\sigma_H=30^\circ$ ) and uniform azimuth plane distribution [24] .....	33

## List of Figures

Figure 2-18 Distribution parameters giving constant MEG (-3dB) of dipole antennas regardless of the antenna orientation [24] .....	34
Figure 3-1 Simulated fading signal power for $N=50$ , $\beta=0.2$ .....	39
Figure 3-2 Histogram of the simulated fading signals: real-part, imaginary-part and amplitude. Gaussian and Rayleigh PDF curves are also plotted for comparison.....	39
Figure 3-3 Autocorrelation of the complex fading signals simulated for $\beta=0.2$ ; Clarke reference model is also plotted for comparison for $f_d$ supposed to be 0.1 .....	40
Figure 3-4 Simulated Cross-correlation of the real and imaginary-part of fading for $\beta=0.2$ and the reference model.....	40
Figure 3-5 Autocorrelation of the modeled fading signal for $\beta=0.1, 0.2, 0.3, 0.4, 0.5$ versus time lag .....	41
Figure 3-6 Simulated cross-correlation of the fading signal for $\beta=0.1, 0.2, 0.3, 0.4, 0.5$ versus time lag.....	42
Figure 3-7 Indoor measurement setup for antenna performance evaluation in multipath environment using random field method.....	49
Figure 3-8 Random field measurement using electromagnetic wave scatters.....	49
Figure 3-9 Random field measurement setup inside metallic shielded chamber .....	50
Figure 3-10 Supelec, large mode stirred reverberation chamber model.....	52
Figure 3-11 Supelec large reverberation chamber photograph; The large metallic chamber, Network analyzer, and personal computer for controlling the rotating stirrer are illustrated .....	53
Figure 3-12 Number of modes versus frequency (MHz) generated inside the Supelec MSRC .....	53
Figure 3-13 Rotating paddle model installed inside MSRC (Top) isometric and top view (bottom) the paddle photograph .....	55
Figure 3-14 Supelec mode stirred reverberation chamber model (top view), the placement of the rotating paddle and working zone are illustrated.....	56
Figure 3-15 Measurement setup for chamber statistical parameters evaluation including large reverberation , transmitting monopole antenna, receiving dipole antenna and network analyzer .....	58
Figure 3-16 Measured fading signal magnitude (normalized to mean) and phase inside MSRC for one revolution of the stirrer for 900, 1800, 2450 and 5100 MHz bands respectively; the receiving antenna installed inside the working volume of the chamber ...	60
Figure 3-17 Normalized intensity moments (semi logarithmic scale) relevant to the amplitude of fading signal versus their order; (a) frequency 900MHz (b) frequency 1800MHz (c) frequency 2450MHz (d) frequency 5100MHz .....	63

## List of Figures

Figure 3-18 Autocorrelation function of the measured signals versus samples shift (a) frequency: 900MHz (b) frequency: 1800MHz (c) frequency: 2450MHz (d) frequency: 5100MHz.....	64
Figure 3-19 Measured power samples normalized to mean with and without decimation; frequency: 900MHz, decimation rate: 1/25.....	65
Figure 3-20 ACF of the measured signals at 900MHz after applying the decimation factor of 1/25 on the raw measured data.....	66
Figure 3-21 The histogram of the measured signals amplitude and the Rayleigh matched density functions(a) frequency: 900MHz (b) frequency: 1800MHz (c) frequency: 2450MHz (d) frequency: 5100MHz.....	67
Figure 3-22 CDF plot of the measured signals amplitude and the reference Rayleigh distribution (constructed from a Rayleigh distributed population with the same parameter as the measured data) (a) frequency: 900MHz (b) frequency: 1800MHz (c) frequency: 2450MHz (d) frequency: 5100MHz.....	68
Figure 3-23 Measured probability distribution function plot of the in-phase, quadrature and phase components of the fading signals for the test frequencies for 900,1800,2450 and 5100MHz.....	69
Figure 3-24 Measured and simulated autocorrelation of the fading signals for the complex, real and imaginary parts respectively (a)-(c). The cross-correlation of the fading is also illustrated in (d). The measurements are performed for 2450 MHz and the best matched results of the simulation is given for $\beta=0.05$ .....	71
Figure 3-25 Uniformity of the average power distribution as a function of the stirrer positions at the operating frequencies for 900MHz, 1800MHz, 2450MHz and 5100MHz..	72
Figure 3-26 Measured PDF of the XPR (dB) for 2450MHz. The distribution is Gaussian with $m= -0.23$ dB.....	73
Figure 3-27 Measured signal power versus recording time for three revolution of the rotating paddle; frequency: 900MHz.....	74
Figure 3-28 Autocorrelation function of the measured signals versus time shift (sec) for three revolution of the rotating stirrer .....	74
Figure 4-1 correlation between the envelopes of signals received on two horizontally separated base station antennas as a function of the field arrival angle $\alpha$ . (—) $\alpha=5^\circ$ , (- - -) $\alpha=10^\circ$ , (----) $\alpha=20^\circ$ , (-.-.) $\alpha=30^\circ$ , (- - -) $\alpha=60^\circ$ , (- - - -) $\alpha=90^\circ$ [3].....	80
Figure 4-2 Diversity reception systems: (a) selection (b) equal-gain (c) maximum ratio, combining.....	82
Figure 4-3 Cumulative distribution probability of output CNR (dB) for selection combining for various diversity orders (M) .....	83
Figure 4-4 Cumulative probability distribution of output CNR (dB) for maximum ratio combining (MRC) for various diversity orders.....	84
Figure 4-5 CDF plot of the output CNR for two-branch diversity system for SC, MRC and EGC.....	86

## List of Figures

Figure 4-6 Diversity gain for maximum ratio combining and selection combining for two-branch diversity system for 0.1 and 0.01 CDF levels [50].....	88
Figure 4-7 Diversity gain versus correlation coefficient and branches power imbalance for (a) SC, (b) EGC and (c) MRC based on equations given in (4-6).....	89
Figure 4-8 LCR and AFD: LCR is the average number of positive-going crossing per second, AFD is the average of $\tau_1, \tau_2, \dots, \tau_n$ .....	90
Figure 4-9 Normalized LCR and AFD versus normalized signal level (dB) for two branch diversity system.....	91
Figure 4-10 Two vertically polarized radiating antennas representation in spherical coordinate system with distance $d$ .....	97
Figure 4-11 Correlation coefficient between two vertically polarized isotropic antennas versus separation distance $d(\lambda)$ ; AoAs are given by Taga model for $m_\theta=0^\circ$ and $\sigma_\theta$ values..	98
Figure 4-12 Correlation coefficient between two vertically separated antennas with distance $d$ ; AoAs are given by Taga model for $m_\theta=0^\circ$ and $\sigma_\theta$ values.....	99
Figure 4-13 Two horizontally spaced antennas in a multipath channel with Gaussian distributed field angle of arrivals with dispersion angle of $\sigma$ and $m_\theta$ .....	100
Figure 4-14 Correlation coefficient versus spatial separation for two vertically polarized antennas; the incident field is considered, uniform in the azimuth plane and Gaussian in the elevation with $\sigma_\theta=1^\circ$ and various $m_\theta$ .....	100
Figure 4-15 Correlation coefficient between two isotropic radiating antennas versus separation distance. The antennas are exposed to scattering field with Clarke model for field AoA distribution.....	101
Figure 4-16 Correlation coefficient between two isotropic radiating antennas versus separation distance. The antennas are exposed to scattering field with isotropic field AoA distribution.....	102
Figure 4-17 Correlation coefficient computation error versus number of uncorrelated signal samples .....	103
Figure 4-18 Computed received signal power using two isotropic antennas with separation distance of $d=0.3\lambda$ and the signal variation rate for $\beta=0.1$ .....	103
Figure 4-19 CDF plot of the normalized signal powers (dB) in the diversity branches ( $P_1$ and $P_2$ ) and after combining; the receiving antennas are isotropic and are separated with distance $0.3\lambda$ .....	104
Figure 4-20 Diversity gain versus separation distance for two isotropically radiating antennas and various signal combining techniques. The probability level $\alpha$ is 0.1.....	105
Figure 4-21 Diversity gain versus separation distance ( $\lambda$ ) for two isotropically radiating antennas and various signal combining techniques. The probability level $\alpha$ is 0.01.....	105
Figure 4-22 Diversity gain (dB) versus correlation coefficient for $\alpha=0.01$ and for selection, equal gain and maximum ratio combining. The best fitted curve is also illustrated for each case of combining.....	106

## List of Figures

Figure 4-23 Diversity gain (dB) versus correlation coefficient for $\alpha=0.1$ and for selection, equal gain and maximum ratio combining. The best fitted curve is also illustrated for each case of combining.....	106
Figure 4-24 CDF plot of the simulated signals in diversity branches ( $P_1$ ) and after signals combining for various correlation coefficient. (a) selection combining (b) maximum ratio combining.....	108
Figure 4-25 Diversity gain against correlation coefficient and power imbalance for $\alpha=0.1$ ; (Left) SC and (Right) MRC.....	109
Figure 4-26 Diversity gain against correlation coefficient and power imbalance for $\alpha=0.01$ ; (Left) SC and (Right) MRC.....	110
Figure 4-27 Measurement setup inside reverberation chamber for spatial correlation test.	112
Figure 4-28 correlation coefficient between spatial points measured inside reverberation chamber; square envelop of the complex correlation, correlation between signals voltage and correlation between signals power are illustrated.....	114
Figure 4-29 Measured and computed correlation coefficient between two spatial points with distance $d$ .....	115
Figure 4-30 Simulated spatial correlation coefficient versus distance in an isotropically scattering field channel. Two antenna types are used: isotropic radiation antenna and dipole antenna.....	116
Figure 4-31 Measured and theoretical normalized LCR versus normalized signal powers	116
Figure 4-32 Measured and theoretical AFD versus normalized signal power .....	117
Figure 5-1 correlation coefficient as a function of antenna spacing: a comparison of Japanese workers' experimental results [56].....	120
Figure 5-2 Two parallel (half-wave) dipole antennas horizontally separated with distance $d$ .....	123
Figure 5-3 Envelop correlation coefficient between two half-wave dipoles with separation distance $d$ ; (---) computed from antenna element factor (—) Clarke's function.....	123
Figure 5-4 Simulated and measured mutual power coupling between two dipole antennas versus separation distance ( $\lambda$ ).....	124
Figure 5-5 Farfield radiation power pattern of two parallel dipole antennas for different separation distances for a) $d=0.1\lambda$ , b) $d=0.2\lambda$ and c) $d=0.4\lambda$ and for each antenna port excitation when the other antenna is matched to $50\Omega$ impedance.....	125
Figure 5-6 Correlation coefficient as a function of antenna spacing (wavelengths), simulated and measured inside an isotropically scattered field environment. (---) Theory calculated; (...) overall simulated; (—) simulated using pattern-amplitude diversity effects; (-·-·-) simulated using pattern-phase diversity effects; (-o-) overall measured inside mode stirred reverberation chamber .....	126
Figure 5-7 Simulated antenna prototype used for illustrating the pattern-phase diversity effects .....	128

## List of Figures

Figure 5-8 phase difference between radiation patterns versus spatial angles ( $\theta, \varphi$ ); a) The phase diversity generated, $\Delta\Phi$ ( $\Omega$ ), between two coupled dipole antennas with separation distance $d=0.1\lambda$ ; b) an equivalent phase difference generated due to space diversity ( $\beta d \cos\varphi \sin\theta$ ) for $d=0.2\lambda$ .....	129
Figure 5-9 Reverberation chamber measurement setup for two port signal acquisition .....	130
Figure 5-10 Measured signal power at the diversity antenna ports for $d=0.2\lambda$ .....	131
Figure 5-11 CDF of the measured signal powers inside MSRC for dipoles separation distance $d=0.2\lambda$ : $P_1$ and $P_2$ are the measured signal powers in the diversity branches; $P_{SC}$ and $P_{MRC}$ are the signal powers after diversity combining: SC and MRC, respectively; $P_{Single}$ is the signal power received with a single antenna with no antenna close to it .....	133
Figure 5-12 Measured apparent diversity gain (dB) versus dipole separation ( $\lambda$ ) for selection combining (SC) and maximum ratio combining (MRC) at 0.1 CDF level .....	133
Figure 5-13 Measured effective diversity gain (dB) versus dipole separation ( $\lambda$ ) for selection combining (SC) and maximum ratio combining (MRC) at 0.1 CDF level .....	134
Figure 5-14 Simulated radiation efficiency degradation (dB) and measured mean signal power degradation (dB) in diversity configuration compared to single dipole antenna, versus separation distance ( $\lambda$ ) .....	135
Figure 5-15 (a) simulated diversity gain versus dipoles distance for SC and MRC and $\alpha=0.1$ , $\alpha=0.01$ . (b) a sample CDF for $d=0.2\lambda$ is illustrated .....	136
Figure 5-16 Single port pattern diversity antenna structure using two impedance loaded parasitic dipoles .....	137
Figure 5-17 Simulated radiation pattern of dipole diversity system for $d=0.15\lambda$ , and a) $Z_1=\infty, Z_2=0$ b) $Z_1=0, Z_2=\infty$ .....	138
Figure 5-18 Farfield radiation pattern of parasitic diversity configuration for $Z_1=-20j \Omega$ (left) and $Z_1=-100j \Omega$ (right) .....	139
Figure 5-19 (a) Sagem myc-2 mobile photograph (b) Antenna diversity prototype developed using two helical antennas .....	141
Figure 5-20 modeled handset diversity antenna and the Sagem helical antenna prototype .....	141
Figure 5-21 Return loss and mutual power coupling (dB) for helical antennas versus frequency (MHz) (a) measured (b) Simulated model given in Figure 5-20 .....	143
Figure 5-22 Satimo spherical anechoic chamber test bed and the AUT position inside the chamber .....	144
Figure 5-23 Left) simulated Right) measured farfield power gain (dBi) versus $\theta$ and $\varphi$ spherical angles; antenna 1 is excited and antenna 2 is loaded by $50\Omega$ impedance (see Figure 5-20). Frequency: 938MHz .....	145
Figure 5-24 Left) simulated Right) measured farfield power gain (dBi) versus $\theta$ and $\varphi$ spherical angles; antenna 1 is excited and antenna 2 is loaded by $50\Omega$ impedance (see Figure 5-20); Frequency: 938MHz .....	145

## List of Figures

Figure 5-25 Simulated farfield patterns of the mobile diversity antennas in spherical coordinate system. The bolded line indicate 3dB beamwidth (GSM band).....	145
Figure 5-26 Computed envelop correlation coefficient in the GSM band based on the simulated and the measured radiation patterns.....	148
Figure 5-27 Diversity gain (dB) for different AoAs and combining techniques based on the <i>simulated</i> pattern in the GSM band Left) $\alpha=0.1$ Right) $\alpha=0.01$ .....	149
Figure 5-28 Diversity gain (dB) for different AoAs and combining techniques based on the <i>measured</i> pattern in the GSM band Left) $\alpha=0.1$ Right) $\alpha=0.01$ .....	150
Figure 5-29 CDF of the modeled signals in the diversity branches and after combining: SC, EGC and MRC .....	150
Figure 5-30 Normalized LCR of the modeled signals of the diversity antenna with and without signals combining: SC, EGC and MRC. The Rayleigh LCR is compared to the simulations.....	151
Figure 5-31 Simulated farfield patterns of the mobile diversity antennas in spherical coordinate system. The bolded line indicate 3dB beamwidth (DCS band).....	151
Figure 5-32 Diversity gain (dB) for different AoA models and combining techniques based on the <i>simulated</i> pattern in the DCS band (a) $\alpha=0.1$ (b) $\alpha=0.01$ .....	152
Figure 5-33 Measured signal power samples in the diversity branches for (Left) GSM and (Right) DCS bands .....	153
Figure 5-34 Measured CDF plot of the signal power in the diversity branches ( $P_1$ and $P_2$ ), and after signals combining ( $P_{SC}$ , $P_{EGC}$ and $P_{MRC}$ ). The CDF of the signals in the case with one helical antenna is also illustrated ( $P_{Single}$ ). Frequency 938MHz.....	154
Figure 5-35 Measured CDF plot of the signal power in the diversity branches ( $P_1$ and $P_2$ ), and after signals combining ( $P_{SC}$ , $P_{EGC}$ and $P_{MRC}$ ). The CDF of the signals in the case with one helical antenna is also illustrated ( $P_{Single}$ ). Frequency 1800MHz.....	155
Figure 5-36 Diversity antenna prototype at the presence of the head phantom .....	156
Figure 5-37 Measured signal power samples in the diversity branches at the presence of the human head phantom for (Left) GSM and (Right) DCS bands.....	156
Figure 5-38 Measured CDF of the signal powers in the diversity branches ( $P_1$ and $P_2$ ), and after combining ( $P_{SC}$ , $P_{EGC}$ and $P_{MRC}$ ) at the presence of the human head phantom. (Left) GSM band (Right) DCS band .....	157
Figure 5-39 Measured diversity gains for SC, EGC and MRC with and without phantom human head for the GSM and DCS frequency bands (Left) $\alpha=0.1$ (Right) $\alpha=0.01$ .....	158
Figure 5-40 Local envelop correlation coefficient for spatial angles $\Omega(\theta, \varphi)$ by considering $XPR=1$ .....	160
Figure 5-41 Local envelop correlation coefficient computed from the measured azimuth plane radiation patterns; $XPR= 0, 3, 6$ dB.....	161
Figure 6-1 Circular patch antenna with two feed points at $P_1$ and $P_2$ ; $a=17.5\text{mm}$ , $r=0.66a$	165

## List of Figures

Figure 6-2 Simulated and measured return loss (for P1) and coupling for dual feed circular patch antenna; simulations are conducted using MOM (IE3D) and TLM (Flomerics)full wave electromagnetic solution codes .....	167
Figure 6-3 Farfield pattern of the circular patch antenna (a) $\theta$ -polarized, top view (b) $\phi$ -polarized top view and (c) total field, for P1 and P2 excitations. The bolded line shows the 3dB beamwidth.....	168
Figure 6-4 Simulated signal samples in the diversity antenna branches for XPR=1; the autocorrelation of the fading is also illustrated .....	169
Figure 6-5 Simulated CDF of the fading signals in the diversity branches (P1,P2) and after signals combining: selection, equal gain and maximum ratio.....	169
Figure 6-6 Measured signal samples in the diversity antenna branches inside MSRC; the autocorrelation of the fading is also illustrated .....	170
Figure 6-7 CDF of the measured signal powers in the diversity branches (P <sub>1</sub> ,P <sub>2</sub> ) and after signals combining: selection, equal gain and maximum ratio.....	171
Figure 6-8 simulated and measured diversity gain of the polarization diversity system and the equivalent diversity gain based on space diversity systems .....	171
Figure 6-9 Aperture coupled patch and slanted dipoles over an infinite ground plane investigated by Lindmark [13] .....	172
Figure 6-10 3-D FFC magnitude of the circular patch polarization diversity antenna versus spatial angles .....	172
Figure 6-11 Antenna diversity gain (dB) for (a) SC and (b) MRC versus $\theta$ and $\phi$ spatial angles for $\alpha=0.01$ level and XPR=1 .....	173
Figure 6-12 Top) Farfield radiation pattern of the circular patch polarization diversity antenna; (Bottom) farfield pattern for ACP (Left) and Slanted dipoles (Right) [13].....	174
Figure 6-13 FFC magnitude of the polarization diversity antennas for the azimuth plane (a) circular patch (b) ACP and 45° slanted dipoles [13].....	175
Figure 6-14 local envelop correlation coefficient ( $\rho_e$ ) for XPR=0, 3, 6, 9 dB; Top) the circular patch antenna (Bottom) ACP and slanted dipoles [13].....	175
Figure 6-15 Diversity gain of the circular patch antenna for 0.01 level (a) selection combining (b) maximum ratio.....	176
Figure 6-16MRC diversity gain at the 0.01 level for XPR = 0 and 6 dB using the ACP and dipole elements [13].....	177
Figure 6-17 A single port antenna diversity prototype with switching elements and the related patterns [71].....	179
Figure 6-18 pattern diversity antenna with switching elements on a cylindrical ground base [81] .....	180
Figure 6-19 (a) A 16-element circular configuration in which seven elements are short circuited. The beam can be steered around in 22.5° steps. The radius for the example here is 0.25 $\lambda$ . (b) The farfield power pattern for the 16-element configuration [74].....	181

## List of Figures

Figure 6-20 (a) The modeled pattern diversity antenna on a finite ground plane with 16-parasitic elements. (b) Return loss versus frequency for single monopole on the ground plane and after installing the parasitic elements .....	182
Figure 6-21 Different wire meanderline antennas on a circular ground plane .....	183
Figure 6-22 Simulated return loss of the meander, dual meander and the dual meander with open ended antenna configurations .....	183
Figure 6-23 (a) current distribution along the dual-meander antenna with open circuit configuration, (b) radiation pattern of the antenna .....	184
Figure 6-24 Meander line antenna with parasitic switched elements; A) antenna diversity prototype B) dual-meander antenna on the ground plane C) Switch parasitic elements positions: ( ) short circuited elements and ( ) open circuited elements are illustrated .....	185
Figure 6-25 Constructed antenna photograph; eight rods are screwed to the ground base and the others are raised with 1mm above the ground .....	186
Figure 6-26 Measured and simulated return loss (dB) versus frequency (GHz).....	187
Figure 6-27 Simulated 3-D power pattern (dBi) versus azimuth and elevation angles; (a) Positive y-axis rods are switched to the ground plane; (b) Negative y-axis rods are switched to the ground.....	188
Figure 6-28 CDF of the simulated signals in the pattern diversity antenna port and after selection combining.....	189
Figure 6-29 Measured CDF of the signal powers (dB), normalized to mean, by the pattern diversity antenna with and without applying the switching among the parasitic elements.	191
Figure 6-30 (a) Geometry of Y-patch antenna with diversity ability (b) reduced size patch antenna [82] .....	193
Figure 6-31 Notched Pentagonal Strip antenna structure .....	193
Figure 6-32 (a) 3D view of the diversity antenna (b) NPS antenna and the two current paths between the antenna ports .....	194
Figure 6-33 surface current density on the NPS antenna and the excited ports; the resonating strips have the maximum current and are depicted in the figure .....	195
Figure 6-34 Optimized geometry of the NPS antenna for operating in 2450MHz and wide-band characteristics .....	196
Figure 6-35 Photograph of the manufactured NPS antenna .....	196
Figure 6-36 Measured and computed return loss (dB) versus frequency (GHz); the computed values are given for MOM and TLM full-wave electromagnetic solutions .....	197
Figure 6-37 Measured and computed coupling (dB) versus frequency (GHz); the computed values are given for MOM and TLM full-wave electromagnetic solutions .....	197
Figure 6-38 Simulated 3-D pattern of the NPS antenna (Top view and isometric view) (a) P <sub>1</sub> (b) P <sub>2</sub> excitations .....	198

## List of Figures

Figure 6-39 Measured 3-D farfield patterns of the NPS antenna (a) Port 1 excitation (b) port 2 excitation (c) top view of both patterns. Measurements are conducted in Supelec spherical base anechoic chamber.....	199
Figure 6-40 Self-impedance and mutual impedance (resistance $r_{ij}$ and inductance $x_{ij}$ ) computed from the measured S-parameters .....	200
Figure 6-41 Estimated signals correlation coefficient (based on mutual impedance) versus frequency .....	200
Figure 6-42 Simulated CDF of the fading signals in the diversity branches ( $P_1, P_2$ ) and after signals combining: selection, equal gain and maximum ratio.....	201
Figure 6-43 Measured fading signals in NPS antenna diversity branches ( $P_1$ and $P_2$ ) .....	202
Figure 6-44 CDF plot of the measured signals in diversity branches and after combining techniques: selection, equal gain and maximum ratio.....	202
Figure 6-45 Antenna diversity prototype including: printed patch on FR4 substrate material, two coaxial lines and a rectangular shaped metallic ground plane.....	205
Figure 6-46 Simulated RMS current distribution on the strip antenna regarding to the excited ports at 2450 MHz; high dense (red) colors show the resonating parts.....	206
Figure 6-47 Measured and simulated return-loss (for one port) and coupling (dB) versus frequency (GHz).....	207
Figure 6-48 Simulated 3-D farfield radiation power pattern gains (dBi) versus $\theta$ and $\varphi$ (spherical coordinate angles left) $P_1$ is excited right) $P_2$ is excited .....	208
Figure 6-49 CDF plot of the computed signal powers in the diversity antenna branches and the signal powers after combining; selection, equal gain and maximum ratio.....	209
Figure 6-50 Measured fading signals in the trapezium shaped antenna branches.....	210
Figure 6-51 CDF plot of the measured signals in the antenna ports and after combining: SC, EGC and MRC .....	210
Figure 6-52 Measured diversity gain enhancement for circular patch, NPS and trapezium shaped antennas for the signals combining and $\alpha=0.1$ level .....	212
Figure 6-53 Measured diversity gain enhancement for circular patch, NPS and trapezium shaped antennas for the signals combining and $\alpha=0.01$ level .....	212

## List of Tables

Table 2-1 Jakes family fading simulator parameters.....	17
Table 2-2 Best fit parameters to the elevation plane distribution models based on double exponential distribution [25] for both “ $\theta/\varphi$ ” polarizations.....	25
Table 2-3 Mathematical and empirical scattering field distributions for different wireless environments: $M_1$ is a 2-dimensional model referred to Clarke; $M_2$ and $M_3$ consider uniform AoA distribution in azimuth, Gaussian and double exponential in elevation plane; $M_4$ is Gaussian distribution in the elevation plane and elliptical distribution for the azimuth plane .....	27
Table 2-4 Measured XPR of the various multipath fading environments at 2145MHz [25]	29
Table 3-1 Supelec reverberation chamber statistical test results at different operating frequencies and antenna location; Decimation factor indicates the sampling rate reduction factor to generate uncorrelated data; the measured and reference $\chi^2$ values are tabulated. If the measured value less than reference one the null hypothesis (i.e. the Rayleigh model) is not rejected. ....	66
Table 3-2 Measured mean and variance of the real and imaginary parts of the fading signals for frequencies for 900~5100MHz inside working volume and one location near to chamber wall .....	70
Table 4-1 <i>PDF</i> , <i>CDF</i> and the mean of the <i>CNR</i> for single branch Rayleigh channel and for the diversity branches with selection, equal gain and maximum ratio combining abilities ..	83
Table 4-2 Equations express the variations of the AFD and LCR for Rayleigh channels and for the channels after diversity combining (diversity order, $M=2$ ). $R_n=R/R_{rms}$ and $R$ is the specified level.....	91
Table 4-3 Parameters showing the coefficients of the equation (4-19) for the best fitted curves to the diversity gain plot versus correlation coefficient and for linear combining techniques.....	107
Table 5-1 Antenna diversity performance for GSM band based on the <i>Simulated</i> patterns. Signals correlation coefficient and diversity gain for $\alpha=0.1$ and $\alpha=0.01$ are tabulated. $M_0$ - $M_4$ are related to field AoA models.....	147
Table 5-2 Antenna diversity performance for GSM band based on the <i>Measured</i> patterns. Signals correlation coefficient and diversity gain for $\alpha=0.1$ and $\alpha=0.01$ are tabulated. $M_0$ - $M_4$ are related to field AoA models.....	147
Table 5-3 Antenna diversity performance for <i>DCS</i> band, based on the <i>Simulated</i> patterns. Signals correlation coefficient and diversity gain for $\alpha=0.1$ and $\alpha=0.01$ are tabulated. $M_0$ - $M_4$ are related to the field AoA models.....	152
Table 5-4 Measured mobile antenna diversity performance factors: signals correlation coefficient and diversity gains for SC, EGC and MRC for $\alpha=0.1$ and $0.01$ probability levels. The results are provided with and without the effects of the phantom human head .....	154
Table 6-1 Measured and simulated diversity antenna parameters.....	170

## List of Tables

Table 6-2 Measured and simulated correlation coefficient and diversity gain for switch combining.....	189
Table 6-3 Measured and simulated diversity antenna parameters; measurements are conducted in Supelec MSRC; the simulations are based on the computed complex pattern .....	201
Table 6-4 Measured and simulated diversity performance factors for trapezium shaped antenna; frequency: 2450MHz .....	209

# Chapter 1

## Introduction

Next generation mobile phones will be multimedia terminals providing not only speech transmission, but also internet access, video, music, games, etc. With the introduction of new features in mobile terminals higher data rates are required. Indoor is a typical place for high speed data users and therefore performance enhancing features are welcome for indoor environments. This has been recognized for 3rd generation mobile systems, where several new performance enhancement features are introduced by applying transmit antenna diversity, fast power control, soft handover and adaptive antennas. All of these features have the major part of complexity at the base station, by trying to improve the quality of the received signal at the handset terminal.

As an addition or alternative performance enhancement features, multiple antenna systems in hand portable equipment can be used, which will be investigated in this thesis.

While investigating antenna system for hand portable equipment the focus will be on communication performance, which is defined by the parameters that influence the speech quality, data throughput and coverage area that a user will obtain. Furthermore, the data security problems and power consumption of the portable equipment are important.

The communication performance can be specified from the following four variables: system, user profile, antenna and transceiver.

**System:** the key parameters for communication performance is determined by how the network is planned, the number of users in the network and the surrounding radio environment.

**User profile:** the communication performance of a hand portable device is dependent on where it is used and how. The radio environment of the device is characterized by signal strength, polarization, delay spread and interference.

**Antenna:** Nowadays there is mostly single antenna in communication devices used in real environments. By introducing more advanced antenna systems for example, antenna

diversity or smart antennas, multiple input multiple output (MIMO) systems a significant performance enhancement can be obtained.

**Transceiver:** the communication performance of mobile devices is dependent on both antenna system and the transmitter/receiver circuit of the device.

In this thesis we concentrate on the application of antenna diversity for performance enhancing of communication in hand portable equipment. These performances are fast fading mitigation, radio link quality enhancement by increasing the overall received SNR, communication range increment and increased data throughput. The major problem occurring with small equipment is the antenna implementation in small available space. Generally speaking, the minimum quarter-wavelengths separation between antennas is needed for reasonable performance. This issue makes difficult to use the antenna diversity in handset equipment while it will be shown that the assumption is dropped due to some constraints.

To demonstrate the benefits of antenna system with and without diversity it is essential to have a method for evaluating the device. Knowledge of the wave propagation channel characteristics is essential for the performance evaluation. Part of this Ph.D. project has been devoted to the investigation of mobile propagation channels and definition of a laboratory measurement setup for emulating the propagation channel. The other part is the implementation of different compact antenna configurations for diversity reception in mobile handset devices and Wireless LAN equipment.

## **1.1 Objectives for this Thesis**

The project scientific goals are concentrated on the implementation of compact antenna systems in small available space in mobile handset terminals and wireless LAN equipment. Based on that the following topics have been identified for this thesis.

### **Mobile multipath channel investigation and fading simulation**

Mobile multipath fading channels are investigated and fast fading simulators are reviewed. An improved model for mobile fading simulation is presented that has major benefits on the available simulators. The fading simulator is combined with the spherical models of the field angle of arrivals for the mobile multipath channels and a field simulator

is developed. The field simulator is used in the present work for evaluating the antenna unit performance of communication system in the fading channels.

### **Reverberation Chamber for fading emulation**

The antenna performance measurement in real multipath channels is difficult, time consuming and gives different results from one site measurement to the other one. Supelec large reverberation chamber is used in the present work for emulating the multipath fading channels. The statistical characteristics of the fading channel are investigated in detail and are compared to the real mobile fading channels.

### **Multipath fading mitigation techniques using antenna diversity**

Diversity performance enhancement for data communication links is reviewed. The antenna diversity evaluation technique using mutual coupling, radiation pattern, field simulator and signals measurement is investigated. Antenna diversity performance is numerically computed for the space diversity systems. The results are applied to compute the diversity gain for correlated fading channels and imbalanced power in signal branches.

The application of reverberation chamber for antenna diversity test is investigated.

### **Antenna diversity implementation for mobile phones**

The concept of antenna diversity through two parallel dipoles with close spacing is investigated by the radiation pattern theory. A novel diversity technique, “pattern-phase diversity”, is depicted that enhanced the antenna diversity performance for compact prototypes. Based on the research, antenna diversity system for mobile phone is developed and the performance is explored from simulations and the measurements with and without the effects of the head of the handset user.

### **Antenna diversity for wireless LAN applications**

Different compact antennas are designed, simulated, manufactured and implemented for diversity reception for wireless LAN applications. Polarization diversity, pattern diversity and phase diversity are the techniques attached to our prototype antennas. The performances are analyzed from the simulations to the measurements in reverberation chamber. The performances of the various antenna diversity techniques are compared to each other.

## 1.2 Organization of the Thesis

The thesis is organized as follows.

Chapter 2 describes the characteristics of the multipath fading in mobile communication channels. The fading phenomenon is presented and the simulation methods are developed. The mathematical and the empirical field angle of arrival models that are implemented in the present context are studied.

Chapter 3 deals with the definition of a novel technique for fading signals simulation and its development toward field simulator. The field simulator is applied to compute the antenna unite performance of communication systems. The field trial methods are investigated and the reverberation chamber measurements are proposed to replace with the real environment tests. Statistical tools are implemented for characterizing the reverberation chamber.

In chapter 4, we have concentrated on the performance enhancement of the antenna diversity techniques. Some concepts on the diversity gain, signals correlation coefficient and evaluation methods are developed. The reverberation chamber performance dealing with the antenna diversity are measured and presented.

Chapter 5 describes the diversity techniques available using two parallel dipole antennas. A novel diversity technique is depicted for closely spaced antennas that enhances the performance of antenna diversity system. Mobile phone diversity is developed based on these finds.

Chapter 6 presents four novel type antenna diversity prototypes. These antennas are developed for providing polarization, pattern and phase diversity. The antennas design procedure, simulation using full wave electromagnetic solution codes and performances evaluation through computation and measurements are presented.

A list of publications for the project is at the end of this section.

## Publications

1. A.Khaleghi, A.Azoulay, J.C.Bolomey; N. Ribiere-Tharaud “Design and Development of a Compact WLAN Diversity Antenna For Wireless Communications”, 13th International Symposium on Antennas/ JINA 2004, 8-10 November 2004, Nice- France
2. A.Khaleghi, A.Azoulay, J.C.Bolomey; “A Diversity Antenna For 3G Wireless Communications”, IEEE AP-S/URSI 2004, June 2004, Monterey, USA (extended abstract)
3. A.Khaleghi, A.Azoulay, J.C.Bolomey; “Polarization Diversity Performance of a Circular Patch Antenna for Wireless LANs Applications”, VDE- 11th European Wireless Conference 2005, April 10-13, 2005, Nicosia, Cyprus
4. A.Khaleghi, A.Azoulay, J.C.Bolomey; “A Dual Band Back Coupled Meanderline Antenna for WLAN Applications” , IEEE 61st Vehicular Technology Conference (VTC’05), 29th May - 1st June 2005, Stockholm, Sweden
5. A.Khaleghi, A.Azoulay, J.C.Bolomey; ”Diversity Antenna Characteristics Evaluation in Narrow Band Rician Fading Channel Using Random Phase Generation Process” IEEE 61st Vehicular Technology Conference (VTC’05), 29th May - 1st June 2005, Stockholm, Sweden
6. A.Khaleghi, A.Azoulay, J.C.Bolomey; “Far-Field Radiation Pattern Analysis of a Circular Patch Antenna with Polarization Diversity for Wireless Applications” , 11<sup>th</sup> international symposium on Antenna Technology and Applied Electromagnetics (ANTEM 2005), 5-18 June 2005, Saint-Malo – France
7. A.Khaleghi, A.Azoulay, J.C.Bolomey; ”Diversity Techniques with Dipole Antennas in Indoor Multipath Propagation”, 16th Annual IEEE International Symposium on Personal Indoor and Mobile Radio Communications (PIMRC 05), September 11 - 14, 2005, Berlin, Germany
8. A.Khaleghi, A.Azoulay, J.C.Bolomey; “Dual Band Diversity Antenna System for Mobile Phones”, 2<sup>nd</sup> IEEE International Symposium on Wireless Communication Systems 2005 (ISWCS2005), September 5-7, 2005, Siena, Italy
9. A.Khaleghi, J.C. Bolomey, A. Azoulay; “A Pattern Diversity Antenna with Parasitic Switching Elements for Wireless LAN Communications” 2<sup>nd</sup> IEEE International Symposium on Wireless Communication Systems 2005 (ISWCS2005), September 5-9, 2005, Siena, Italy
10. A.Khaleghi, J.C. Bolomey, A. Azoulay; N. Ribiere-Tharaud “A Compact and Broadband Diversity Antenna for Wireless LAN Applications”, 2<sup>nd</sup> IEEE International Symposium on Wireless Communication Systems 2005 (ISWCS2005), September 5-7, 2005, Siena, Italy
11. A.Khaleghi, J.C. Bolomey, A. Azoulay; “On the Statistics of the Reverberation Chambers and Application for Wireless Antenna Test” IEEE conference on the Antennas and propagation (AP-S) 2006, Albuquerque, NM

# Chapter 2

## Multipath Fading Characterization

### 2.1 Introduction

In this chapter, we will describe the basic problem of multipath propagation and its consequences on signal reception. Mobile propagation as well as indoor propagation is mainly affected by reflection and scattering from the surfaces of the building and by diffraction over and/or around them. The energy arrives via several paths simultaneously and a multipath situation is said to exist in which the various incoming radio waves arrive from different directions with different time delays. They combine vectorially at the receiver antenna to give a resultant signal which can be large or small depending on the distribution of phases among the component waves. Moving the receiver by a short distance can change the signal strength by several tens of decibels because the small movement changes the phase relationship between the incoming component waves. Substantial variations therefore occur in the signal amplitude. The signal fluctuations are known as fading and the short term fluctuations caused by the local multipath is known as *fast fading* to distinguish it from the much longer term variation in mean signal level, known as *slow fading*.

These concepts are explained and the models that describing the signal variations are introduced. The fading simulators are presented that can be replaced by the real measurements and are used directly for radio equipment evaluation with the antenna unit removed. The available empirical and mathematical models of the field angle of arrivals (AoA) are shortly investigated in section 2.9. These models are efficient for computing the Doppler spread of the fading signals in multipath channels and also evaluating the mean effective gain of antennas.

### 2.2 Characterization of Mobile Radio Propagation

In mobile radio communications, the emitted electromagnetic waves often do not reach the receiving antenna directly due to obstacles blocking the line-of-sight path. In fact, the received waves are a superposition of waves coming from all directions due to reflection,

diffraction, and scattering caused by buildings, trees, and other obstacles. This effect is known as *multipath propagation*. Figure 2-1 illustrates some possible mechanisms by which energy can arrive at a mobile antenna. Three basic mechanisms impact signal propagation in a mobile communication system. They are reflection, diffraction, and scattering [1].

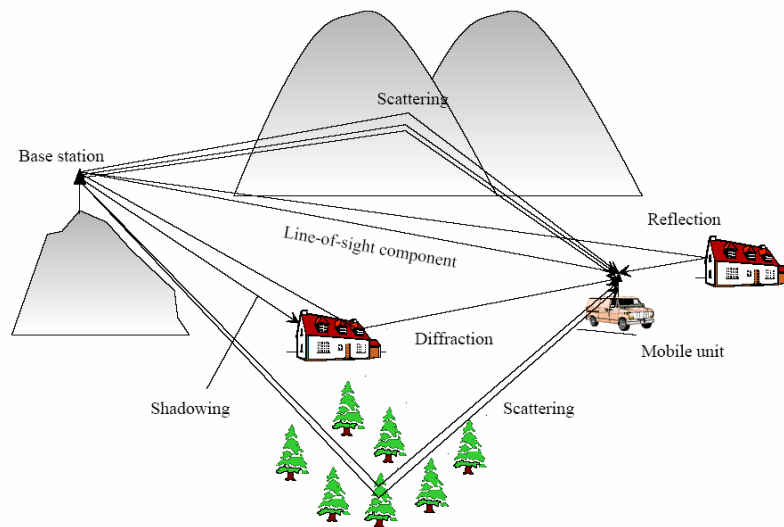


**Figure 2-1 Typical mobile radio scenario illustrating multipath propagation in a terrestrial mobile radio environment [1]**

- *Reflection* occurs when a propagating electromagnetic wave impinges on a smooth surface with very large dimensions compared with the RF signal wavelengths ( $\lambda$ ).
- *Diffraction* occurs when the propagation path between the transmitter and receiver is obstructed by a dense body with dimensions that are large when compared with  $\lambda$ , causing secondary waves to be formed behind the obstructing body. Diffraction is a phenomenon that accounts for RF energy traveling from transmitter to receiver without an LOS path between the two. It is often termed shadowing because the diffracted field can reach the receiver even when shadowed by an impenetrable obstruction.
- *Scattering* occurs when a radio wave impinges on either a large rough surface or any surface with dimensions on the order of  $\lambda$  or less, causing the energy to be spread out (scattered) or reflected in all directions.

In an urban environment, typical signal obstructions that yield scattering are lampposts, street signs, and foliage. The name scattered applies to any obstruction in the propagation path that causes a signal to be reflected or scattered. The major problems in built-up areas

Moving the receiver by a short distance or any variations at the environment can change the signal strength by several tens of decibels because the relative movement changes the phase relationship between the incoming component waves. Substantial variations therefore occur in the signal amplitude. The signal fluctuations are known as *fading*. Two types of fading effects are distinguished that characterize mobile communications: large-scale fading (*slow fading*) and small-scale fading (*fast fading*).

Large-scale fading represents the average signal power attenuation or the path loss resulting from motion over large areas. Because the variations are caused by the mobile moving into the shadow of hills, forests, billboards, or clumps of buildings, slow fading is often called *shadowing*. Measurements indicate that the mean path loss closely fits a log-normal distribution with a standard deviation that depends on the frequency and the environment. For this reason the term *log-normal fading* is also used.

The short-term fluctuation caused by the local multipath is known as fast fading. Fast fading refers to the dramatic changes in signal amplitude and phase that can be experienced as a result of small changes (as small as half wavelengths) in the spatial positioning between a receiver and a transmitter. Fast fading is called Rayleigh fading if there are multiple reflective paths that are large in number, and there is no line-of-sight (LOS) signal component; the central limit theorem can be invoked to model the fast fading by a filtered complex Gaussian process. The envelope of such a received signal is statistically described by a Rayleigh probability density function (PDF).

When a dominant non fading signal component present, such as a LOS propagation path, the statistics of small-scale fading envelope is described by a Rician PDF [2]. In other words, the small-scale fading statistics are said to be Rayleigh whenever the LOS path is blocked, and Rician otherwise.

A mobile radio roaming over a large area must process signals that experience both types of fading: small-scale fading superimposed on large-scale fading. A typical received signal envelope as a function of distance is shown in Figure 2-4 illustrates this point. The slow variation in mean signal level, indicated in Figure 2-4 by the dotted line, occurs over much larger distances. Large-scale fading (attenuation or path loss) can be considered to be a spatial average over the small scale fluctuations of the signal. It is generally evaluated by averaging the received signal over at least 10 to 30 wavelengths to decouple the small-scale

indeed travel in an approximately horizontal direction, because the two-dimensional model successfully explains almost all the observed properties of the signal envelope and phase. Nevertheless, there are differences between what is observed and what is predicted, in particular the observed envelope spectrum shows differences at low frequencies and around  $2f_m$  ( $f_m$  is the maximum Doppler frequency).

An extended model due to Aulin [5] attempts to overcome this difficulty by generalizing Clarke's model so that the vertically polarized waves do not necessarily travel horizontally, i.e. it is a three-dimensional model. The detailed mathematical analysis showing the scattering field distribution effects on the construction of fading are available in [3] and [6]-[7].

## 2.6 Fading Models

Statistical models are commonly employed to characterize stochastic channels when the number of multipaths is large. In this part we briefly discuss about fading models that are used to describe the wireless channels.

At every receiving point it is assumed that the signal to be the resultant of  $N$  plane waves. A typical component wave is shown in Figure 2-5, which illustrates the frame of reference. The  $n^{\text{th}}$  incoming wave has an amplitude  $E_n$  and a phase  $\Phi_n$  with respect to an arbitrary reference, and spatial angles of arrival  $\varphi_n$  and  $\theta_n$ . All of these parameters are statistically random and independent. The mean square value of the amplitude  $E_n$  is

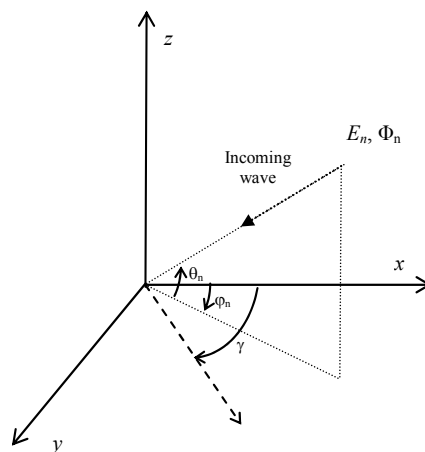


Figure 2-5 Spatial frame of reference:  $\varphi$  is in the horizontal plane (xy- plane);  $\theta$  is in the vertical plane

### 2.6.1 Rayleigh fading model

If  $N$  in equation (2-2) is sufficiently large (theoretically infinite but in practice greater than 6 [3]) then by the central limit theorem the quadrature components  $I(t)$  and  $Q(t)$  are independent Gaussian processes which are completely characterized by their mean value and autocorrelation function. Because the mean values of  $I(t)$  and  $Q(t)$  are both zero, it follows that  $E\{E(t)\}$  is also zero. Further,  $I(t)$  and  $Q(t)$  have equal variance ' $\sigma^2$ ' equal to the mean square value (the mean power).

Practical radio receivers do not normally have the ability to detect the components  $I(t)$  and  $Q(t)$ , they respond to the envelope and/or phase of the complex signal  $E(t)$ . The envelope  $r(t)$  of the complex signal  $E(t)$  is given by

$$r(t) = \sqrt{I^2(t) + Q^2(t)} \quad (2-8)$$

and it is well-known that the PDF of  $r(t)$  is given by [3]

$$p_x(r) = \frac{r}{\sigma^2} \exp\left(-\frac{r^2}{2\sigma^2}\right) \quad (2-9)$$

in which  $\sigma^2$ , is the mean power and  $r^2/2$  is the short-term signal power. This is the Rayleigh density function. Figure 2-6 shows the PDF of the Rayleigh function.

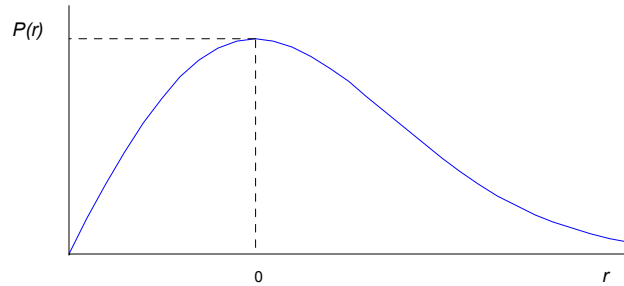


Figure 2-6 PDF of the Rayleigh distribution

The received signal phase  $\Theta(t)$  is given in terms of  $I(t)$  and  $Q(t)$  by

$$\Theta(t) = \tan^{-1}\left(\frac{Q(t)}{I(t)}\right) \quad (2-10)$$

The argument leading to the conclusion that the envelope is Rayleigh distributed also shows that the phase is uniformly distributed in the interval  $[0, 2\pi)$ , i.e.

Many different approaches have been used for the modeling and simulation of mobile radio channels. Among them, the well-known mathematical reference model due to Clarke [4] and its simplified simulation model due to Jakes [8] have been widely used for Rayleigh fading channels for about three decades. In this section, we briefly review the mathematical reference models given for fading channels with the attention on the statistical properties of the reference model. This information gives the possibility to compare our improved fading simulator (see chapter 3) with the existent models.

## 2.8 Fading Simulator Models

Consider a frequency non-selective fading channel comprised of  $N$  propagation paths; and uniform field scatter in azimuth plane (Clarke's two dimensional azimuth scattering model) the low-pass fading process given in equations (2.5) and (2.6) by considering that  $\theta_n=0$ ,  $\omega_n=\omega_d \cos(\gamma-\phi_n)$  are expressed as

$$I(t) = \sum_{n=1}^N E_n \cos(\omega_d t \cos \alpha_n + \phi_n) \quad (2-14)$$

$$Q(t) = \sum_{n=1}^N E_n \sin(\omega_d t \cos \alpha_n + \phi_n) \quad (2-15)$$

where  $\alpha_n = \gamma - \phi_n$  and  $\phi_n$  is uniformly distributed over  $[0, 2\pi)$ .  $\omega_d$  is the maximum radian Doppler occurring when  $\alpha_n=0$ .

Assuming that  $\alpha_n$  and  $\phi_n$  are mutually independent and uniformly distributed over  $[0, 2\pi)$ , some desired second order statistics for fading simulators are manifested in the autocorrelation and cross-correlation functions as [9]

$$R_{I,I}(\tau) = E[I(t)I(t+\tau)] = J_0(\omega_d \tau) \quad (2-16a)$$

$$R_{Q,Q}(\tau) = E[Q(t)Q(t+\tau)] = J_0(\omega_d \tau) \quad (2-16b)$$

$$R_{Q,I} = R_{I,Q} = 0 \quad (2-16c)$$

$$R_{r,r} = J_0(\omega_d \tau) \quad (2-16e)$$

Despite the extensive acceptance and application of Jakes simulator, some important limitations of the simulator were determined and discussed in detail recently [10]. It was shown that Jakes' simulator is wide-sense non-stationary when averaged across the physical ensemble of fading channels [11]. Some improvements in Jakes' simulation model proposed that permits to generate uncorrelated fading waveforms and resolve the WSS non-stationary problem of the Jakes model [10] and defined as Jakes simulators family. Among the Jakes simulator family, the recently improved model proposed by Pop and Beaulieu in [6] is worthy of mention due to its wide-sense stationary. In this simulator the normalized low-pass fading process of the improved Jakes simulator proposed as

$$u(t) = u_c(t) + ju_s(t) \quad (2-20a)$$

$$u_c(t) = \frac{2}{\sqrt{N}} \sum_{n=0}^M a_n \cos(\omega_n t + \phi_n) \quad (2-20b)$$

$$u_s(t) = \frac{2}{\sqrt{N}} \sum_{n=0}^M b_n \cos(\omega_n t + \phi_n) \quad (2-20c)$$

where  $a_n, b_n, \beta_n$  and  $\omega_n$  are the same as those of Jakes original model given in Table 2-1, and  $\phi_n$  is independent random variables uniformly distributed on  $[-\pi, \pi)$  for all  $n$ . the second order statistics of these simulators are analytically given in [11]. In this part we calculate a fading channel based on the above presented models. Figure 2-7 to Figure 2-9 show the

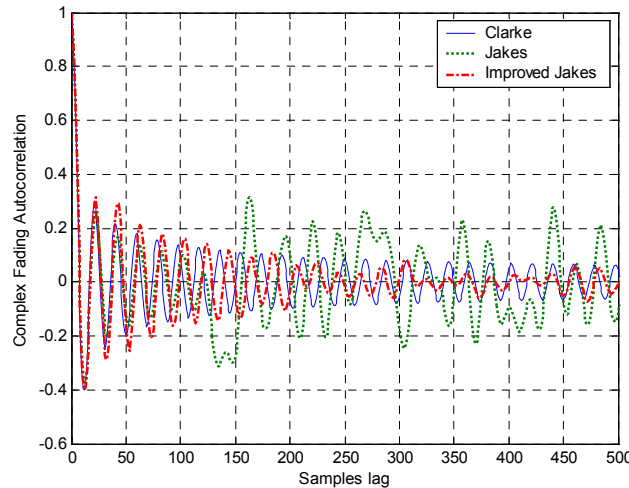


**Figure 2-7 Comparison among autocorrelation of the simulated complex fading; Jakes model, improved Jakes model and Clarke reference model**

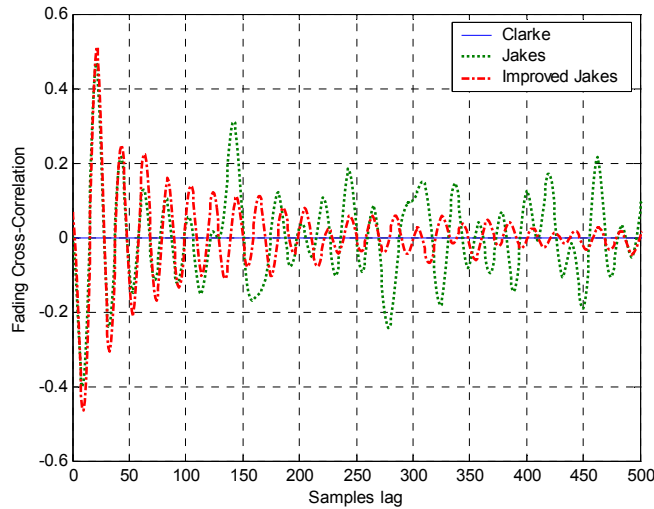


**Figure 2-10 Comparison among cross-correlation of the simulated fading signals; Jakes model, improved Jakes model and Clarke reference model (note that the reference model is always zero)**

autocorrelation of the real and imaginary parts and the autocorrelation of the complex fading, based on the different simulators are in accordance with the Clarke reference model. The cross-correlation of the real-imaginary parts of the fading is non zero and is different from the Clarke reference.

## 2.9 Empirical and Mathematical AoA Models

The fading simulators based on Clarke and Jakes have assumed two-dimensional model for the scattering fields. In mobile radio reception, signals typically arrive at the receiver antenna from a wide range of directions due to multipath propagation. This can be described by *angle of arrival* (AoA) distribution of the fields in the propagation environment. Knowing the AoA distribution, the Doppler spectrum and the signals autocorrelation function can be directly computed [22]. The power spectral density of the fading signals depends on the PDFs associated with the spatial angle of arrivals. In this case the limits of the Doppler spectrum can be quite high compared to Clarke two dimensional model given by equation (2-17). The Doppler information must be provided in the design of transceivers used in hand-portable equipment. Furthermore, design and implementation of antennas for mobile communication instruments need the knowledge of AoAs. Mean effective gain (MEG) as an issue showing the average received power by mobile antenna in fading environment, and diversity antenna performance need the AoA information. To compute these issues the AoA

Figure 2-12 shows the form of the RF power spectrum of the fading signals for the field AoAs as Clarke model and the AoAs as Aulin model. The results for an improved Aulin model is also provided [3] (not discussed here).

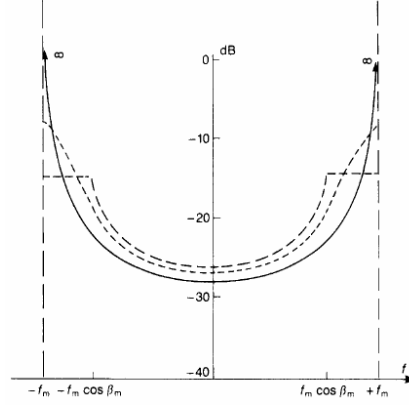


**Figure 2-12 Form of the RF power spectrum using different scattering models: (—) Clarke's model, (---) Aulin's model, (- - -) improved Aulin model;  $\theta_m=45^\circ$  [3]**

Several empirical AoA distributions for the incoming field are proposed from measurements and correspond to the local surrounding of the mobile propagation environments. For the simplicity, these models assume that the power spectrum has been modeled in elevation and azimuth separately and combined according to

$$P_{\theta}(\theta, \varphi) = P_{\theta}(\theta)P_{\varphi}(\varphi) \quad (2-22a)$$

$$P_{\varphi}(\theta, \varphi) = P_{\varphi}(\theta)P_{\varphi}(\varphi) \quad (2-22b)$$

where  $P_{\theta}(\theta)$ ,  $P_{\varphi}(\theta)$  are the power spectrums in elevation and  $P_{\theta}(\varphi)$ ,  $P_{\varphi}(\varphi)$  are the power spectrums in azimuth for  $\theta$  and  $\varphi$  polarization, respectively. All of the distributions introduced here assume Rayleigh fading, where neither line of sight (LOS) nor strong contributions to the total scattered field is present. Most of these distributions consider a uniform field at the azimuth plane.

The first empirical model propose an isotropically scatters in space for both polarizations and both azimuth and elevation angles

$$P_{\theta, \varphi}(\theta) = P_{\theta, \varphi}(\varphi) = \begin{cases} A_0 & 0 \leq \theta < \pi, 0 \leq \varphi < 2\pi \\ 0 & \text{Otherwise} \end{cases} \quad (2-23)$$

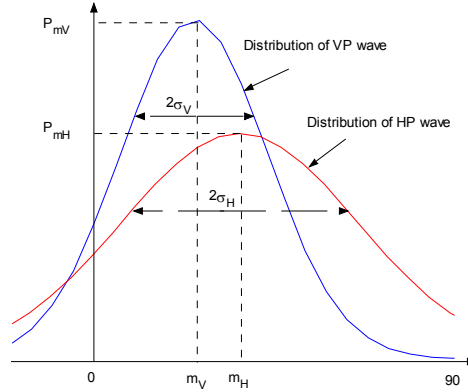


**Figure 2-13 Two truncated Gaussian functions corresponds to field elevation plane AoA distributions in urban environments**

Pederson [26] in his paper proposed a *Laplacian* distribution for AoAs in the elevation plane. He has shown that better fit to the measured AoA directions can be obtained using Laplacian function instead of Gaussian function proposed by Taga. The distribution function for outdoor environments is proposed as

$$P_{\theta,\varphi}(\theta) = A_{\theta,\varphi} \exp\left[-\frac{\sqrt{2}|\theta - m_{v,H}|^2}{\sigma_{v,H}}\right], \quad -\frac{\pi}{2} < \theta \leq \frac{\pi}{2} \quad (2-26)$$

The model assumes a uniform distribution of the fields for the azimuth angles.

Another interesting model proposed by *Kalliola* [25] was to consider a uniform distribution in azimuth and a non symmetrical General double exponential in elevation. He proposed this model instead of Gaussian distribution; better accordance for the measurements has been reported compared to the Gaussian model. The field power distribution at the elevation angles is expressed as

$$P_{\theta,\varphi}(\theta) = \begin{cases} A_1 \exp\left[-\frac{\sqrt{2}|\theta - \theta_0|}{\sigma^-}\right] & \theta \in \left[-\frac{\pi}{2}, \theta_0\right] \\ A_2 \exp\left[-\frac{\sqrt{2}|\theta - \theta_0|}{\sigma^+}\right] & \theta \in \left[\theta_0, +\frac{\pi}{2}\right] \end{cases} \quad (2-27)$$

where  $\theta_0$  is peak elevation angle measured from horizontal, and  $\sigma$ ,  $\sigma^-$  and  $\sigma^+$  control the spread of the functions. Coefficients  $A_1$  and  $A_2$  are set to satisfy unity integral of truncated distribution (see equation (2-26)). The related parameters for the proposed model at different

where  $a_{\theta 1}$  and  $b_{\theta 1}$  are the axial ratios of the ellipsis and  $b_{\theta 0}$  gives the directivity towards the windows. A similar distribution is assumed for the horizontal polarization with corresponding parameters  $a_{\phi 1}$ ,  $b_{\phi 1}$ ,  $b_{\phi 0}$  and  $A_{\phi}$ . It is observed that a uniform distribution is a special case of the elliptical model. Due to the measurements performed by *Knudsen* [27] the elliptical parameters are given as:

$$\begin{aligned} a_{\theta 1} &= 0.71, b_{\theta 0} = 0.70, b_{\theta 1} = 2.12 \\ a_{\phi 1} &= 0.98, b_{\phi 0} = 0.46, b_{\phi 1} = 1.18 \end{aligned} \quad (2-28b)$$

Furthermore, in this model the field power distribution in elevation plane was considered as Gaussian distribution.

In this thesis the above propagation models have been applied to cover as much as possible of the indoor, outdoor and outdoor to indoor propagation scenarios. The models are used for the mean effective gain and diversity performance factors evaluation. Table 2-3 summarizes the applied propagation models in this thesis.  $M_1$  corresponds to Clarke 2-D model with AoA in azimuth plane only.  $M_2$  corresponds to a model with uniform field distribution in azimuth plane and Gaussian in elevation (Gaussian parameters given in Table 2-3 correspond to Taga's model);  $M_3$  considers a uniform distribution in azimuth plane and Double exponential in elevation the related parameters are depicted in Table 2-2.  $M_4$  supposes an elliptical distribution in azimuth plane with maximum value toward the building opening and Gaussian distribution in elevation plane. The Gaussian parameters can be adjusted as Taga model.

Figure 2-14a-d illustrate the incident field AoA distributions given in Table 2-3.

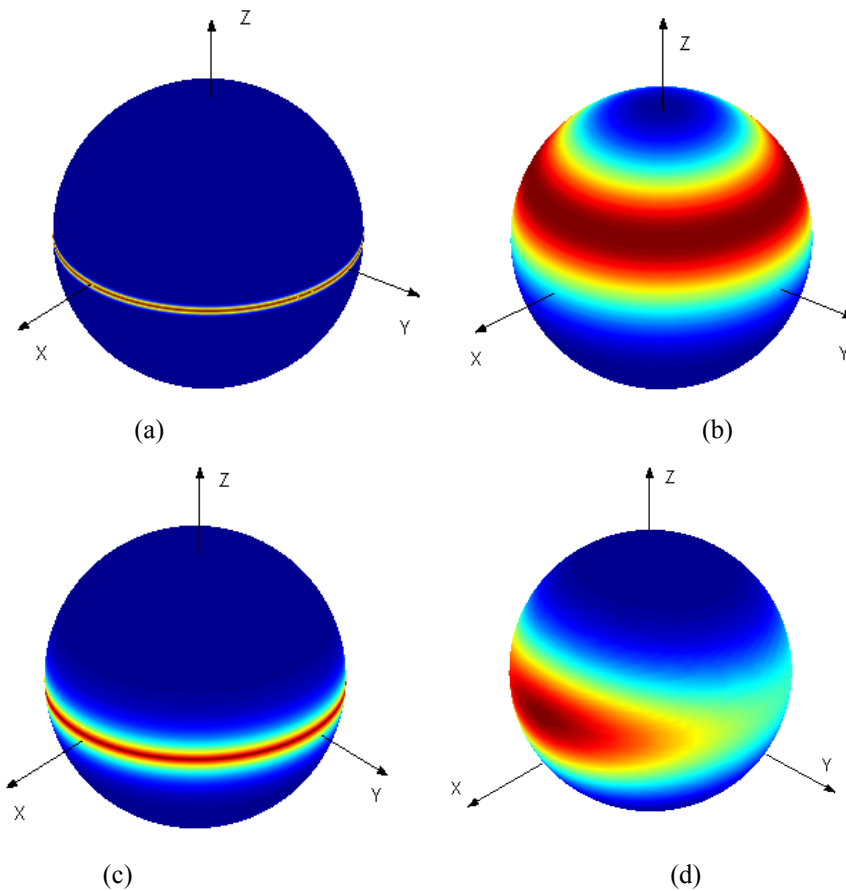


**Figure 2-14** Illustration of the AoA distribution in various multipath propagation channels (a) *Clarke* model  $M_1$ , uniform distribution in azimuth plane only (b) *Taga* model  $M_2$ , Uniform distribution in azimuth and Gaussian distribution in the elevation (c) *Kalliola* model  $M_3$ , Uniform azimuth and double exponential in elevation (d) *Knudsen* model  $M_4$ , Gaussian distribution in elevation and elliptical distribution in azimuth; Red color show high dense scatters

## 2.10 Cross Polarization Power Ratio (XPR)

Clarke and Jake's models consider a vertically polarized incident field on a mobile terminal in a multipath propagation channels. This assumption may be only valid for short distance receiver antenna from the base station. If the separation between the transmitter and receiver increases, the number of depolarizing reflections and diffraction on the propagation path will increase. The field XPR will vary depending on the surrounding environment. The polarization variation in an urban environment may be caused by reflection and/or diffraction rays. However, in an empty room with composite walls, rays are subjected to multiple reflections which could be considered as source of wave depolarization. The XPR has to be known to completely describe the signal environment.

influence on the XPR. In the highway macrocell measurements, the close scattering from the bodywork of the car most probably decreases the XPR. The XPR decreased to 0dB at sites surrounded by tall buildings [24].

### 2.11 Mean Effective Gain (MEG)

Mean Effective Gain is a parameter which shows the performance of an antenna system in relation with the scattering field environment. It is defined as the ratio of the average power received by an antenna in a random scattering field environment to the total average power incident to the antenna in the same environment. The total power is the summation of vertical and horizontal polarized powers that receive by an isotropic antenna. A general formulation for the MEG is expressed as

$$MEG = \frac{\overline{P}_{Rec}}{\overline{P}_V + \overline{P}_H} \quad (2-30)$$

where  $\overline{P}_{Rec}$  is the average power received at the antenna,  $\overline{P}_V$  and  $\overline{P}_H$  are the vertical and horizontal polarized waves received by an isotropic antenna at the same environment of the antenna under test. *MEG* contains the mutual effect between the antenna power gain pattern and the propagation characteristics of the multipath scenario.

Under the assumption that the incident field on the antenna is composed of two uncorrelated vertical and horizontal components, both of a Rayleigh distribution, the received power by an antenna in this environment is given by

$$P_{Rec} = \int_{\Omega} \{P_V G_{\theta}(\Omega) P_{\theta}(\Omega) + P_H G_{\varphi}(\Omega) P_{\varphi}(\Omega)\} d\Omega, \quad \Omega(\theta, \varphi) \quad (2-31)$$

where  $\Omega(\theta, \varphi)$  is the spatial angles in steradian;  $d\Omega = \sin\theta d\theta d\varphi$  and  $G_{\varphi}(\Omega)$ ,  $G_{\theta}(\Omega)$  are the antenna power gains for  $\varphi$ -polarized and  $\theta$ -polarized field components, respectively;  $P_V$  and  $P_H$  are the mean incident powers in vertical and horizontal polarizations, respectively.  $P_{\theta}(\Omega)$  and  $P_{\varphi}(\Omega)$  are the  $\theta$ -polarized and  $\varphi$ -polarized components of the angular power density functions of the incoming waves assume the normalization in (2-24).

By dividing the received power of the antenna under test to the incident power on the antenna the mean effective gain is then determined using (2-30) and (2-33) [24],[31] as

omnidirectional radiation pattern, high efficiency, and high cross polarization discrimination.

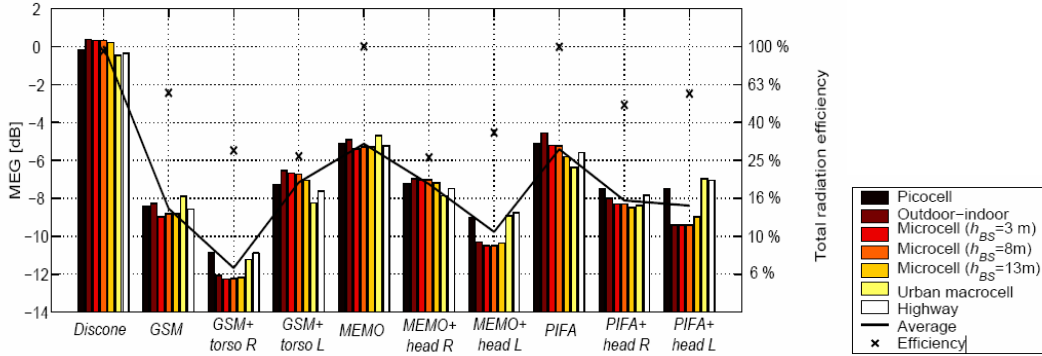


**Figure 2-15 Mean effective gain of evaluated antennas, PIFA, MEMO, Discone in different multipath scattering field environments [25]**

### 2.11.1 MEG measurements

Based on researches conducted by Taga [24], in a Rayleigh multipath fading environment with sufficiently large values of multi trajectories, the  $MEG$  of  $55^\circ$  inclined half-wavelengths dipole antenna is almost constantly equal to  $-3\text{dBi}$ , regardless of the cross polarization power ratio and the statistical power distribution of incident waves. At this angle, the  $VP$  radiation power of the antennas is equal to  $HP$  radiation power.

This can be obtained if the derivative of the  $MEG$  with respect to the  $XPR$  is zero

$$\frac{\partial MEG}{\partial XPR} = 0 \quad (2-34)$$

or by substituting (2-34) in (2-32) we conclude that,

$$\frac{\partial MEG}{\partial XPR} = \frac{\oint (G_\theta P_\theta - G_\phi P_\phi) d\Omega}{(1 + XPR)^2} \quad (2-35)$$

Hence the necessary and sufficient condition is that the total radiated power with  $\theta$ -polarization must equal the total radiated power of the  $\phi$ -polarization [23]. Figure 2-16 shows a half wavelengths dipole antenna inclined with  $\alpha$  degree from the vertical axis. The variation of the  $MEG$  of the dipole antenna is shown in Figure 2-17. At the point A with any arbitrary incident wave distribution parameters ( $XPR, m_V, m_H, \sigma_V, \sigma_H$ ) the variation of  $MEG$

giving constant MEG (-3dBi) characteristics regardless of the antenna orientation, in addition to unusual environment with uniform illumination from all directions. Therefore, it is predicted that there is a possibility of developing an artificial propagation environment where the average received signal level of antennas can be made constant regardless of the orientation of antenna pattern and polarization. It was expected that these environments could be developed by controlling the polarity of the transmitting antenna for XPR, the height of the transmitting antenna for mean elevation angle, and beamwidth of the transmitting antenna for standard deviation [24]. This type of propagation channel was realized inside a Mode Stirred Reverberation Chamber (MSRC) that is our main reference environment for MEG measurements.

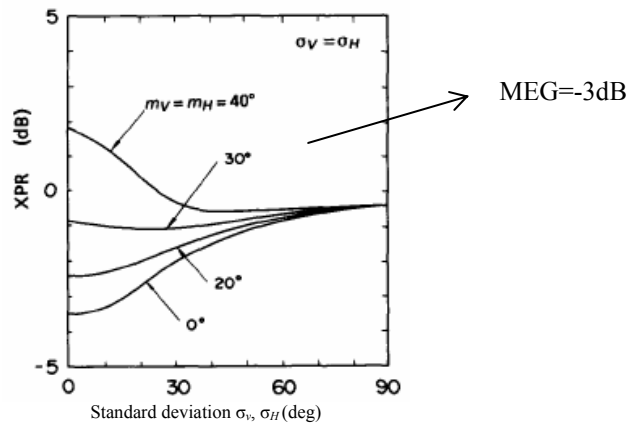


**Figure 2-18 Distribution parameters giving constant MEG (-3dB) of dipole antennas regardless of the antenna orientation [24]**

## 2.12 Summary

In this chapter, the communication over fading channels has been discussed. The short-term fading affects the wireless telecommunication in multipath channels. The fading simulators are investigated that generate the fading signals in the antenna input port with the antenna removed. The simulator is effective for evaluating the radio unit of a communication device without the antenna.

Fading simulator based on Clarke mathematical reference model that corresponds to the real environment measurements is investigated. The first and the second order statistics of the fading are presented. Jakes' simulator family is investigated that provides fading signals

# **Chapter 3**

## **Fading Simulator, Field Simulator and Reverberation Chamber**

### **3.1 Introduction**

In chapter 2 we discussed about the available methods for fading signals generation in the antenna port of a communication system. The method is efficient for radio unit evaluation of communication systems when antenna is removed. In this chapter we have improved a new type of fading simulator that generates the fading signals with quite good accordance with Clarke reference model.

To consider the performance of the antenna unit of a communication system the application of the fading simulator is extended. It is combined with field AoAs for simulating the signals in the antenna ports with the antenna unit effects. This approach is called field simulator to distinguish it from the well-known fading simulator. The field simulator is applied in the present context, for characterizing the mean effective gain of the antennas, signals computation for antenna diversity systems and antenna diversity performance evaluation in multipath fading channels.

Random field trial is an experimental method for measuring the antenna and communication system performance. It can be developed in laboratory environment and can be replaced by the real environment measurements. Reverberation chambers have grown in popularity for electromagnetic immunity (EMI) testing in the last decade. In this thesis, we use Supelec large reverberation chamber for emulating mobile multipath propagation channels. Statistical tools are used for characterizing the random field propagation environment. The reverberation chamber statistical characteristics together with the installed measurement setup give the possibility to use it as laboratory test equipment for measuring mean effective gain, efficiency and diversity performance of the antennas.

Sections 3.6 and 3.9 of this chapter most deal with the description of Supelec large reverberation chamber, chamber excitation, working volume, data acquisition and statistical

where  $\psi_i$  defines the phase of the scattered path (channel) and the amplitude of each scattered channel is unity constant. The term  $1/\sqrt{N}$  is used to normalize the total incident power to unity.  $\Phi_i$  is a random variable term illustrates the manner in which the channel phase is varying. The phase variations can be defined within  $[0, 2\pi)$  or  $[-\pi, \pi)$ ; the phase definition range generate fading signals with different second order statistical characteristics.

The phase term can be selected to be randomly varying with time  $\Phi_i(t)$  or to be a time constant variable  $\Phi_i(t) = \Phi_i(t_0)$ .  $\beta$  is a multiplication factor which controls the effects of the  $\Phi_i$  on the channel phase factor,  $\psi_i(t)$ . It defines the rate of the random channel variation.  $\beta=0$  relates to a time stationary channel and  $\beta=1$  indicates a completely random channel. Adjusting the  $\beta$  within  $[0, 1)$  controls the variation rate of the multipath fading signals and consequently the autocorrelation function of the signals.

The time variations, or dynamic changes in the propagation environment, cause multipath signals variations. This variation can be related directly to the motion of the receiver and indirectly to the Doppler effects that arise. The rate of change of phase, due to motion, is apparent as Doppler frequency shift in each propagation path. Therefore, the  $\beta$  value in equation (3-1c) can be related to the Doppler effects. This case occurs inside the multipath channel of a mode stirred reverberation chamber, where the phase variations are generated by a rotating stirrer; the variations can be related to Doppler frequency in fading simulator systems [12].

Now we examine the statistical properties of the simulated signals,  $X(t)$ , for different constructions of the phase term,  $\psi_i(t)$ . By assuming that  $\psi_i(t)$  is

$$\psi_i(t) = \psi_i(t-1) + \beta \Phi_i \quad (3-2)$$

where  $\Phi_i$  is a random variable uniformly distributed within  $[-\pi, \pi)$  and is independently generated for each random channel ( $i^{\text{th}}$ -path). The initial phase  $\psi_i(t_0)$  is also random uniform selected within  $[-\pi, \pi)$ . Figure 3-1 shows the generated fading signals using equation (3-1b); the signals are constructed for a case with  $N=50$  channel realizations,  $\beta=0.2$  and 5000 time samples. The histogram of the fading signal samples for the real and imaginary parts are illustrated in Figure 3-2. The real and imaginary parts are Gaussian distributed with zero mean values and variance of  $\sigma^2=0.5$ . Consequently, the fading signal amplitude follows

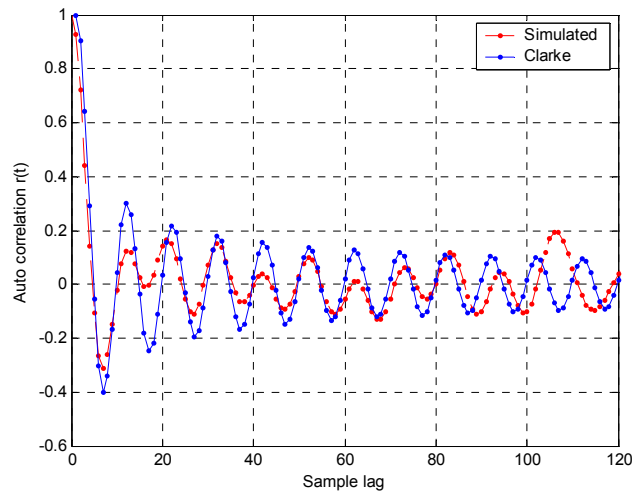


**Figure 3-3 Autocorrelation of the complex fading signals simulated for  $\beta=0.2$ ; Clarke reference model is also plotted for comparison for  $f_d$  supposed to be 0.1**

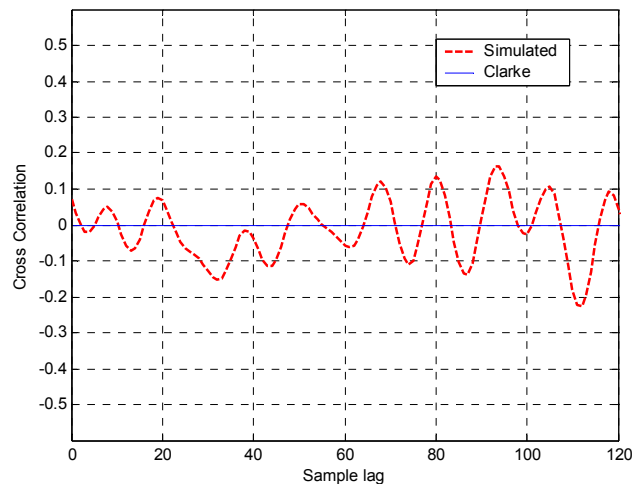


**Figure 3-4 Simulated Cross-correlation of the real and imaginary-part of fading for  $\beta=0.2$  and the reference model**

The cross-correlation between the real and imaginary parts of the fading is plotted in Figure 3-4. As shown the cross-correlation of the simulated fading is varying close to zero and is in accordance with the mathematical reference model. This is one advantage of our fading simulator compared to the Jakes family simulators (see Figure 2-10). Therefore, the improved fading simulator results are more matched to Clarke mathematical reference model. In section 3.9 it is shown that the real environment measurements indicate similar cross-correlation function of the fading signals.

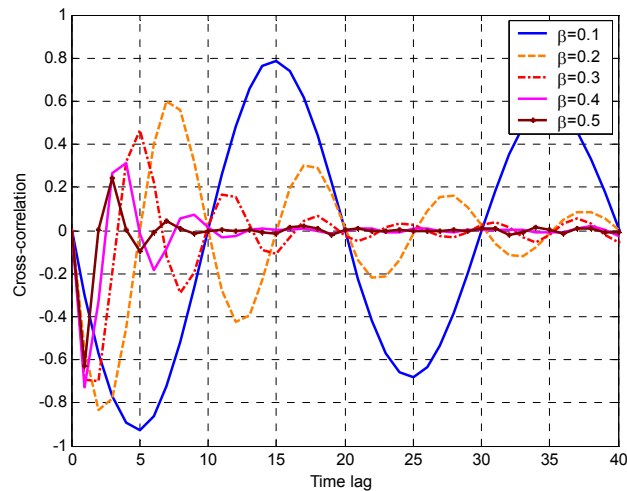


**Figure 3-6 Simulated cross-correlation of the fading signal for  $\beta=0.1, 0.2, 0.3, 0.4, 0.5$  versus time lag**

Among the above proposed fading signals simulation the first method is selected that is more compatible with real environment measurement. The simulator is used in chapter 4 for generating multiple fading signals with a pre-defined signals correlation coefficient. The computed signals are applied to investigate the performance of diversity gain in multi-antenna receiving systems.

### 3.3 Field Simulator

Using the fading simulator described in the previous section, the characteristics of wireless equipment can be evaluated by inputting a fading wave to the antenna input port with the antenna removed. The test is effective for evaluating the radio unit of a communication device without the antenna. However, it is also necessary to confirm the characteristics of the product with the antenna included. In the fading signal simulator the multipath is generated and summed over channels in order to produce the received signal. If the antenna is included in the channel path, depending on the channel spatial direction, different gain and phase values will be applied to each channel. In fact, the antenna will work as a spatial filter with a gain and phase value proportional to the antenna farfield pattern. If the multipath signals pass through the radiation pattern the received signal will include the mutual effect of the channel and antenna unit. In this section we review the available simulation methods for evaluating the received signals by an antenna in a multipath channel.

where  $E_{\theta}^A(\Omega)$  and  $E_{\varphi}^A(\Omega)$  are the antenna complex farfield patterns for  $\theta$ -polarized and  $\varphi$ -polarized field components, respectively. The antenna pattern can be modeled using electromagnetic full-wave solutions or can be measured inside an anechoic chamber. To provide a reference for the received signal power, the incident field on the antenna is normalized and provides unity radiated power on the antenna

$$\int_{\Omega} E_{\theta}^i(\Omega) E_{\theta}^{i*}(\Omega) d\Omega = \int_{\Omega} E_{\varphi}^i(\Omega) E_{\varphi}^{i*}(\Omega) d\Omega = 1 \quad (3-6)$$

and the antenna power patterns are normalized to isotropic

$$\int_{\Omega} \left\{ E_{\theta}^A(\Omega) E_{\theta}^{*A}(\Omega) + E_{\varphi}^A(\Omega) E_{\varphi}^{*A}(\Omega) \right\} d\Omega = 4\pi \quad (3-7)$$

By the present pattern normalization, the effects of the antenna radiation efficiency on the received signal powers are removed.

The received signal by an antenna is a function of both the incident field and the antenna farfield radiation patterns. The antenna radiation pattern is weakly affected by the surrounding environment if sufficiently large distance between the antenna and the surrounding obstacles are considered. For a mobile handheld device, the user head and hand are close to the antenna and both changes the radiation pattern, considerably. Therefore, to have a good estimation of the signals received through an antenna the pattern should be evaluated regarding to the surrounding environment effects. Considering that the antenna pattern is evaluated rigorously in relation with the near environments and no pattern changes are made by the obstacles, we could conclude that the received signal variations by the time at the antenna port is directly influenced by the environment temporal variations or by the antenna displacement in different locations.

To simulate the random multipath signals received at an antenna port one method is proposed by Rice [20] that was based on a developed propagation model [21]. This model provides the statistical characterizations of the number, amplitude, time-delay, and arrival angle of the different components of the multipath signal. Using a Monte Carlo approach, random variables were generated based upon the model for each of the four parameters mentioned above. Each multipath component was then treated as a plane wave whose direction of propagation, amplitude, and phase were controlled by the appropriate random

$$E_{\theta}^i(\Omega, t) = r_{\theta}(\Omega) e^{-j\psi_{\theta}(\Omega, t)} \hat{\theta} \quad (3-9a)$$

$$E_{\varphi}^i(\Omega, t) = r_{\varphi}(\Omega) e^{-j\psi_{\varphi}(\Omega, t)} \hat{\varphi} \quad (3.9b)$$

where  $r_{\theta}(\Omega)$  and  $r_{\varphi}(\Omega)$  are the spatial distributions of the field angle of arrivals that are normalized as (3-6) and provide unity incident field power onto the antenna.

To generate a time variable scattered field and consequently a fading signal at the antenna port, we apply the temporal variations onto the phase factor  $\psi_{\theta, \varphi}(\Omega, t)$ . By this method, a random phase is constructed in  $\Omega$  space that is uniformly distributed within  $[0, 2\pi)$ ; the phase factor changes randomly in the time domain. For instance, the phase variation can follow the proposed fading simulator models as (3-1).

By applying the temporal variations of the phase to equation (3-9), the incident field magnitude for each spatial field trajectory it always constant and is equal to  $r(\Omega)$ . In that case the total incident field power on the antenna is determined by  $r(\Omega)$  distribution. Using this method, each multipath component was then treated as a plane wave whose direction of propagation and amplitude are known and the phase is controlled by an appropriate random variables.

The received signal by an antenna in the generated multipath scenario is obtained by multiplying each component by the complex pattern at the appropriate angle and summing the resulting complex components. Normally, the radiation patterns of the antennas can be simulated or measured with a defined angular resolution for spatial angles. Therefore, the integral equation (3-5) that expresses the antenna signals for continues evaluated patterns can be constructed for discrete case as

$$X_c(t_k) = \frac{2\pi}{N} \frac{\pi}{L} \sum_{n=1}^N \sum_{l=1}^L \left( E_{\theta}^i(\theta_l, \phi_n, t_k) \cdot E_{\theta}^{*A}(\theta_l, \phi_n) + E_{\varphi}^i(\theta_l, \phi_n, t_k) \cdot E_{\varphi}^{*A}(\theta_l, \phi_n) \right) \sin \theta_l \quad (3-10)$$

where  $\theta_l = \frac{l\pi}{L}$ ,  $\phi_n = n \frac{2\pi}{N}$  and  $L, N$  are the number of channels in the elevation and azimuth planes, respectively.  $L$  and  $N$  must be selected equal to the resolution of the simulated or measured patterns.  $E^i(\theta_b, \phi_n)$  is the incident field in  $\theta_l$  and  $\phi_n$  directions and  $E^A(\theta_b, \phi_n)$  is the antenna farfield pattern in the related directions. The incident field models are given by equation (3-9). The field amplitude is constant and is defined by the field AoA models; the

relative power can thus be calculated. If the measurements are performed with an operator holding the terminal antenna, the effects of the human body on the measurement are also taken into account. This measurement is thus effective for testing communication devices such as those used on real applications.

The above test and measurements in outdoor environments requires only a suitable transmitting and receiver system and appropriate site of testing. However, the uncertainty of weather conditions from day to day and also the need to obtain a testing license for use of high power transmitter outdoors, makes outdoor testing of mobile terminal troublesome. To overcome these obstacles, a random field measurement system has been developed for indoor usage. The indoor testing method is also good a first test of the AUT before moving on to the final outdoor test.

Figure 3-7 shows a typical indoor measurement setup. The measurement environment is an office/laboratory. The receivers and transmitters are placed at locations marked as  $R_x$ ,  $T_x$ , respectively. Depending on the surrounding furniture, equipment, cabling, the office walls material and shaping, the floor, pillars and outdoor walls, the ceiling and the materials, the placement of the transmitter and receiver different multipath channels are generated. The transmitter is fixed and transmits the signals at the measurement frequency, the receiver (AUT) can be moved in a straight path inside the room or can be rotated around a fixed point. The moving antenna will experience various multipath channels and the measurement can be repeated by periodically movement of the AUT. Ideally, a measuring device with the same number of ports as antennas is needed to measure simultaneously the signals for estimate the multi antenna system performance. Normal network analyzers only have two ports; so a multiplexing system for measuring more than two ports is needed. This is because the terminal may be moving during sampling time and the scattering environment may be changing. Time- multiplexed measurements are acceptable for a static situation in which the scattering environment is unchanging and the terminal remains still over the sample time [32].

in horizontal plane by the inverted L-shaped rotor arm mounted on the pedestal and in the vertical plane by a smaller rotor arm mounted perpendicularly to the first rotor arm. The measurement procedure is the same as that described above. The multipath signals are sampling in time; the mean effective gain and diversity antenna performance is calculated from the received signals. The computation methods will be discussed in Chapter 4.

In situations where test space is even more severely restricted, a measuring system using a compact shielded box can be used. Figure 3-9 shows the measurement setup. In this measurement system, a random electromagnetic field distribution is generated inside the box by means of the reflections off the inner box walls. The AUT is mounted on a rotating pedestal offset from the rotation axis in order to reduce the effects of the terminal antenna directivity on the measurement. The size of the shielded box is small (for instance, 50cm×50cm×100cm). Its operating frequency is above 1GHz. The upper limit of the operating frequency depends on the frequency band of the measurement system. The transmitting antenna is a standard half-wave antenna mounted with the element tilted at a 45° angle to vertical. The AUT is also mounted at a 45° angle on the rotating pedestal. The tilt angle is used to suppress the direct path signal from the transmitter to the receiver [33].

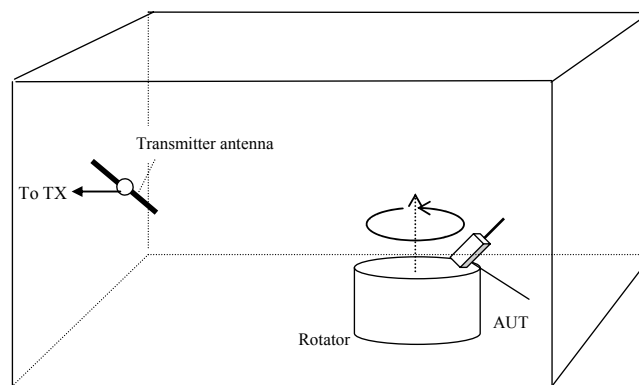


**Figure 3-9 Random field measurement setup inside metallic shielded chamber**

### **3.6 Reverberation Chamber Enclosure**

Reverberation chambers have grown in popularity for electromagnetic immunity (EMI) testing in the last decade. A reverberation chamber generally consists of a rectangular shielded room with metal walls and a mode stirrer, usually in the form of a large paddle, near the ceiling of the chamber. The metal walls of the chamber allow a large field to be

$$f_{m,n,p} = \frac{c}{2} \sqrt{\left(\frac{m^2}{a^2} + \frac{n^2}{b^2} + \frac{p^2}{d^2}\right)} \quad (\text{Hz}) \quad (3-11)$$

$a$ ,  $b$  and  $d$  are the dimensions of the cubic chamber and  $c$  is the velocity of light.  $m$ ,  $n$  and  $p$  are positive integers (only one can be zero).

Due to design constraints, the dimensions of the Supelec mode stirred reverberation chamber are 3 meters long, 1.80 meters wide and 2.40 meters high. Figure 3-10 shows the model of the chamber. It includes one rotating paddle that is installed on the ceiling for modes stirring and multipath generation. The photograph of the reverberation chamber is given in Figure 3-11. The metallic chamber and the measurement instruments are also illustrated on the photo.

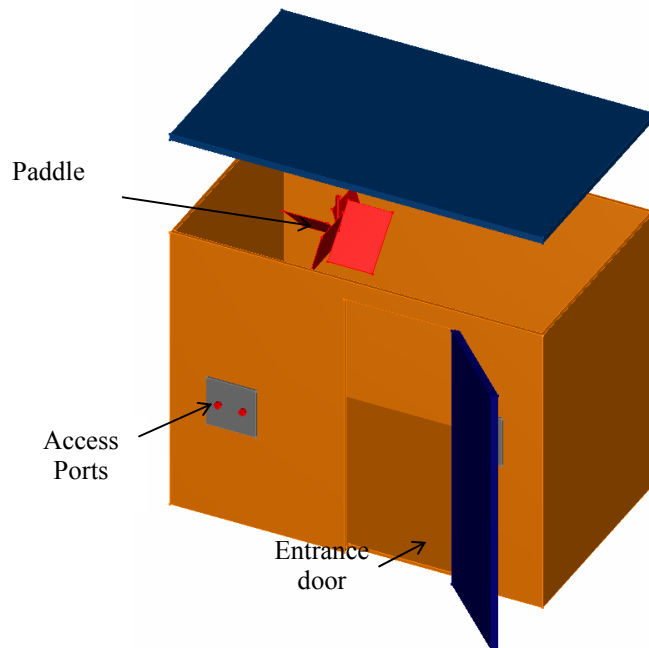


**Figure 3-10 Supelec, large mode stirred reverberation chamber model**

### 3.6.1 Test frequency range

The theoretical lowest usable frequency of the chamber is the frequency above the 60<sup>th</sup> mode [37], so that the stirrer will ‘stir’ the field effectively. The theoretical total number of modes ( $N_S$ ) inside an unperturbed, loss-less, rectangular chamber is dependent on the chamber geometry and can be approximated using the following equation [37]:

### 3.6.2 Antennas

In order to reduce the direct coupling path between the antennas and to maximize the field perturbation, the transmitting antenna (which produces the electromagnetic fields within the chamber) can be directed at the mode stirrer or into the corner of the chamber [38]. Direct coupling is also reduced if the antennas are not too close together and do not face each other [38].

### 3.6.3 Working volume

The working volume is the volume inside which the statistical properties of the MSRC, i.e. homogeneity and isotropy, are respected. As the stirrer rotates, the maximum field obtained during one rotation of the stirrer is the same at any point (greater than 0.5 wavelengths from the chambers walls, floor and ceiling) in the room, this volume is referred to as the *working volume*. The working volume can be found by placing the receiving antenna or a field probe in various positions and monitoring the field strength over one revolution. The actual working volume is determined with a *field monitoring probe*. This probe is used to measure the field strength at any given point within the chamber. After the field strength has been determined for all stirrer positions and various probe positions, calculations can be performed to determine whether the field is statistically uniform at those points for valid tests to be performed and the precise working volume for each frequency can be found.

### 3.6.4 Mode modification techniques

The previous analysis for the number of modes and working frequency were considered a rectangular cubic MSRC without any stirring paddle inside. The performance of the chamber is also depending on the performance of the mode stirrer. The mode stirrer techniques have been investigated such as:

- Rectangular chamber with wall angle irregularities: the intrinsic reverberation chamber (IRC) [39]
- Wall irregularities, such as the phase reflection gratings [40, 41], Schroeder diffusers [42] or corrugated walls [43]
- Moving wall [44]

the paddles were vertically installed, the structure would be symmetric and the multipath signals would be periodic for each  $\frac{1}{4}$  revolution of the stirrer.

The paddle is installed inside the MSRC on the ceiling with 18cm distance from top. The distance from the walls is 90cm. The working zone is presented in Figure 3-14. Throughout the measurement sufficient distance from the walls, ceiling and floor must be considered.

In this context, we use the reverberation chamber as a multipath channel to evaluate our antenna systems, working at GSM, DCS, IEEE 802.11b/g and IEEE 802.11a frequencies at 900, 1800, 2450 and 5100MHz, respectively. Therefore we will study the performance of the chamber in these operating frequencies. The statistical properties of the chamber in relation to frequency and placement of the antenna are investigated in the next section.

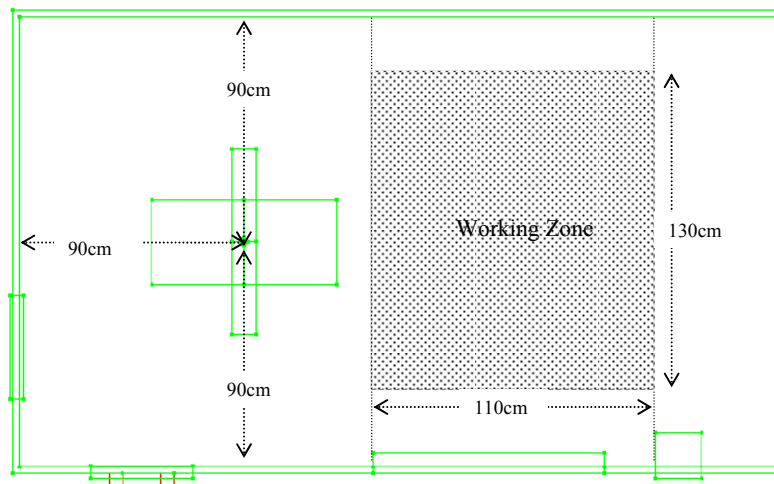


**Figure 3-14** Supelec mode stirred reverberation chamber model (top view), the placement of the rotating paddle and working zone are illustrated

### 3.7 MSRC Excitation and Signal Acquisition

If we use a transmitting antenna inside an MSRC, the multipath is generated by the reflections from the metallic walls and the stirrer. The reflected waves arrive at a point inside the chamber with different magnitudes, due to the number of times the wave was reflected before arriving at the point. The reflected waves have different phase with respect to each other as a result of the different path lengths they have taken to arrive at the point. The revolving stirrer changes the path lengths and the number of reflections of the waves as they

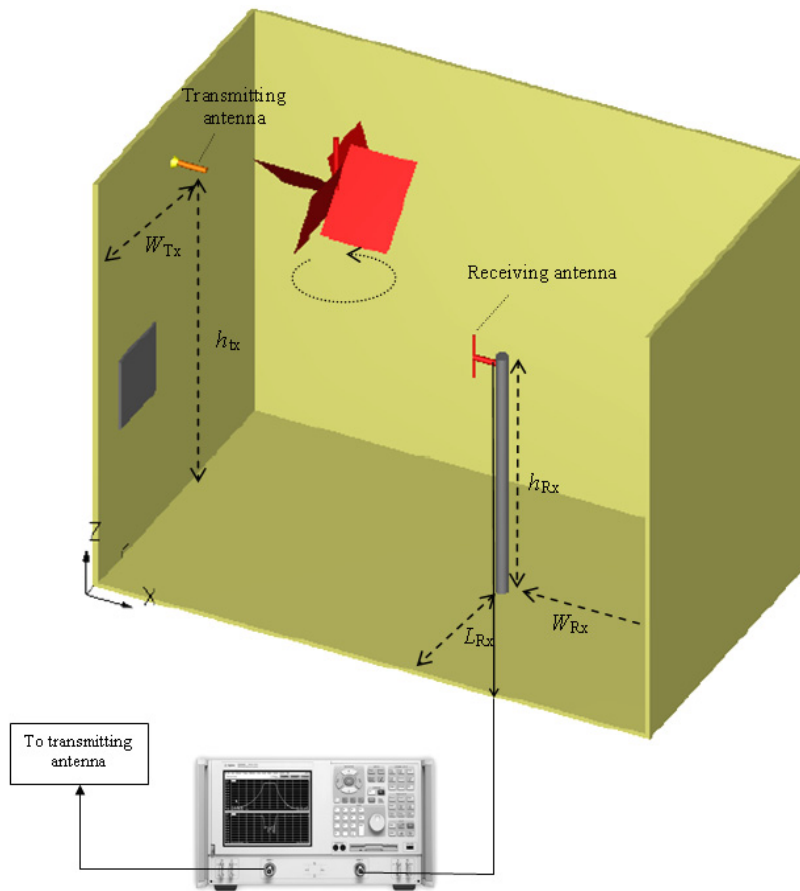


**Figure 3-15 Measurement setup for chamber statistical parameters evaluation including large reverberation , transmitting monopole antenna, receiving dipole antenna and network analyzer**

$W_{Rx}=90$ ,  $L_{Rx}=120$  and  $h_{Rx}=140$ cm. the antenna is inclined about  $45^\circ$  to the vertical axis. The network analyzer is used as both transmitter and receiver, which allows coherent channel sounding. It is set to work in single trace, single frequency and zero span mode for signal acquisition in time domain. The chamber is excited with a continuous wave signal and single frequency, for instance 1800MHz is used; this signal is injected inside the chamber through the transmitting whip antenna. Time variable multipath propagation inside the chamber is made by the rotating stirrer, controlling with a computer code. The stirrer is programmed and is continuously rotating with a constant angular velocity of  $\omega=2\pi/100$  (rad/sec) i.e. one revolution takes 100sec. The received signals are amplitude modulated due to time variable multipath propagation generated by the paddle rotation. The signals amplitude variations are detected by the receiver of the network analyzer (given by scattering parameter  $S_{21}$ ) and the signals are sampled and stored inside the internal buffer of the network analyzer. The

and compared to possible arrangements due to an independent identical distributed sequence [48]. In the reverse arrangements test the monotonic trends, i.e. the persistence, is taken into consideration. Detail in the run test and reverse arrangement tests are given in *Appendix I* of this context.

Once such preliminary steps have been accomplished, it is possible to devise a procedure to estimate the statistics of the underlying phenomena. In order to estimate the first order statistics, many approaches are possible. We consider here three of them: the approach based on the *moment* theorem,  $\chi^2$ -test of hypothesis and *Kolmogorov-Smirnov* test.

The rationale of the first approach is simple: the characteristic function can be described by the moments [49]. Once these moments are known, it is therefore possible to estimate the *PDF* of the underlying process. Of course, in principle, it is requested to evaluate all the moments, while in practice few of them are necessary. Assuming that  $x_1, x_2, \dots, x_N$  are the observed data, we have that the moment of order  $r$  can be estimated by  $M_r = \sum_{i=1}^N x_i^r$  and this estimator is consistent, unbiased, and with variance which depends on the correlation of the observed data [50]. This approach is very simple and useful to provide a first glance estimate of the *PDF*, but it is by no means an asymptotic approach so it is not able to define a confidence level [49].

In the  $\chi^2$ -test the observed data are grouped into non-overlapping cells and compared to the expected ones. The observed data must be independent. The number of the occurrences in a cell needs to be not smaller than five. This test is often employed over the empirical *PDF* (histogram) versus a theoretical one. Where the histogram is itself an estimator of an unknown *PDF*. Whenever the observed data are not grouped, the *Kolmogorov-Smirnov* test should be employed. This test is accomplished on the cumulative distribution function (*CDF*) of the data compared to  $\chi^2$ -test which is performed over the *PDF*. The statistical model underlying such a test requires the data to be independent. In order to measure the independence of the observed data, it is needed to estimate the complex autocorrelation function, since whenever a Gaussian signal is in question decorrelation implies independence. If the data are correlated a decimation factor should be applied to get independent samples.

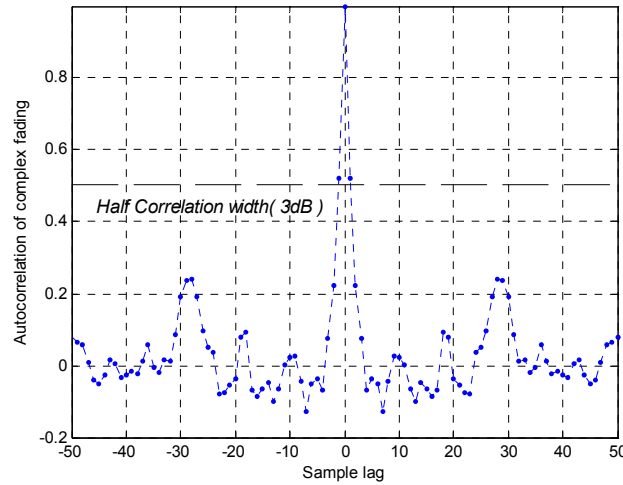


**Figure 3-20 ACF of the measured signals at 900MHz after applying the decimation factor of 1/25 on the raw measured data**

The fading signal is supposed that Rayleigh distributed and the Rayleigh parameter is estimated from the measured signals as

$$\sigma = \sqrt{\frac{1}{2N} \sum_{i=0}^N x_i^2} \quad (3-15)$$

The  $\chi^2$ -test has been applied over the (independent) amplitude of the fading signals to quantitatively measure the goodness of the Rayleigh hypothesis; the confidence level is set to 95%. The average  $\chi^2$ - statistic is computed. This value is compared with the chi-square value from tables [49] for 20 bins at the 95%. If the computed average chi-square statistic is less than the corresponding value from the tables, the hypothesis is accepted. The  $\chi^2$ -test results for different frequencies are tabulated in Table 3-1. All test frequencies passed the  $\chi^2$ -test and

**Table 3-1 Supelec reverberation chamber statistical test results at different operating frequencies and antenna location; Decimation factor indicates the sampling rate reduction factor to generate uncorrelated data; the measured and reference  $\chi^2$  values are tabulated. If the measured value less than reference one the null hypothesis (i.e. the Rayleigh model) is not rejected.**

Frequency (MHz)	Decimation factor	Measured $\chi^2$	Reference $\chi^2$
900	25	15.92	28.86
1800	12	12.26	28.86
2450	11	20.30	28.86
5100	5	19.74	28.86
2450 (near the wall)	11	35	28.86

signals amplitude. The measurement outside the working volume indicates large differences in mean values and this result to the rejection of Rayleigh hypothesis. The mean values close to zero, indicates that the modes are well stirred and there are not any dominant radiated field on the antenna. The best values are indicated for  $f=1800\text{MHz}$  with small mean of the real and the imaginary parts values, in this case the distribution of the phase is more uniform than the others.

**Table 3-2 Measured mean and variance of the real and imaginary parts of the fading signals for frequencies for 900~5100MHz inside working volume and one location near to chamber wall**

Frequency (MHz)	900	1800	2450	5100	2450MHz (near wall)
Mean real	-0.13	0.04	-0.24	0.05	-0.2
Mean Imag.	0.22	0.07	-0.04	0.16	0.5
Variance real	0.58	0.71	0.54	0.69	0.56
Variance Imag.	0.61	0.59	0.64	0.57	0.54

The autocorrelation of the complex, real and imaginary parts of the measured signals together with the cross-correlation of the in-phase and quadrature components for measured faded signals is illustrated in Figure 3-24 a-d. The equivalent simulated results computed using our developed fading simulator by considering the  $\beta$  value of '0.05' is also illustrated for comparison. As shown the measured cross-correlation values vary around zero and the results are comparable to our developed fading simulator model. From Figure 3-24, we could anticipate that the developed fading simulator could emulate the reverberation chamber multipath channel by selecting  $\beta=0.05$  for 2450MHz measurements. For the other measurement frequencies, the  $\beta$  value is proportionally selected. For example, for  $f=5100\text{MHz}$   $\beta$  would be 0.1 and for  $f=1800\text{MHz}$   $\beta$  is selected to 0.036.

One of the results that we obtain from the measurements is the mean signal power at the receiving antenna port. Figure 3-25 illustrates the field strength uniformity versus stirrer positions ( $N_{st}$ ) at the measurement frequencies. The total positions are  $N_{st}=1601$  points for one revolution of the stirrer. As shown, for  $f=1800\text{MHz}$  and  $5100\text{MHz}$  the field average strength is almost stable within  $\pm 0.5\text{dB}$  for  $N_{st}>200$ . For 900MHz and 2450MHz the field average strength is constant for  $N_{st}>800$  positions.

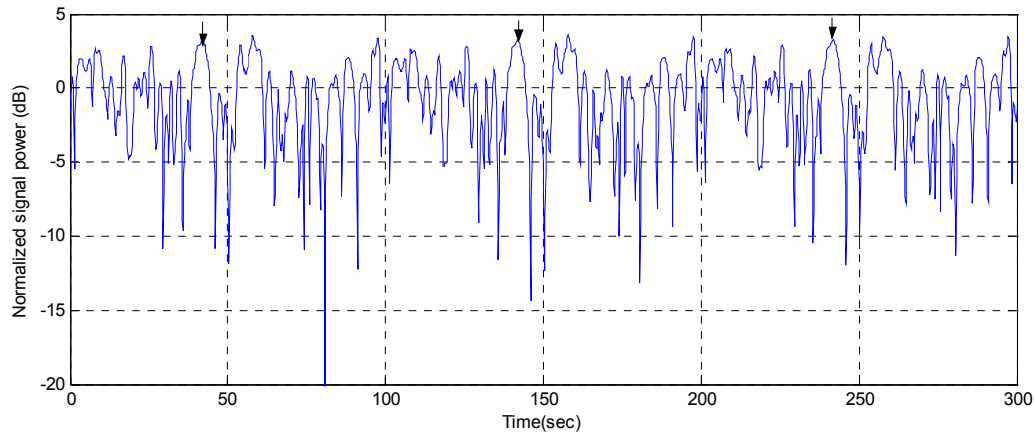


**Figure 3-27 Measured signal power versus recording time for three revolution of the rotating paddle; frequency: 900MHz**

periodically repeated each 100sec. The autocorrelation is useful for finding repeating patterns in a signal. Then the autocorrelation between the signal samples is calculated over total samples. Figure 3-28 shows the measured signals autocorrelation function. For each 100sec, we observe one peak value that indicates the repeating period of the signals. The autocorrelation peak values are reduced by a factor of  $2/3$  and  $1/3$  corresponding to the number of periods used for correlation estimation.

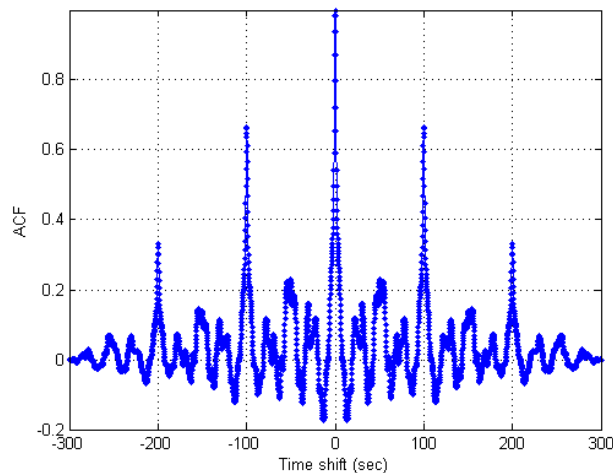


**Figure 3-28 Autocorrelation function of the measured signals versus time shift (sec) for three revolution of the rotating stirrer**

The field periodicity is an important character that offers the possibility of testing the communication devices inside a similar random field environment. Using this facility the measurement of multi-antenna systems is going to be convenient i.e. we are not obliged to

# Chapter 4

## Multipath Fading Mitigation and Antenna Diversity

### 4.1 Introduction

We have seen that buildings and other obstacles in the surrounding environment of a wireless equipment act as scatters of the signal, and because of the interaction between the various incoming component waves, the resultant signal at the receiving antenna is subject to rapid and deep fading. The fading is most severe in heavily built-up areas such as city centers, and the signal envelope often follows a Rayleigh distribution over short distances in these heavily cluttered regions. As the degree of urbanization decreases, the fading becomes less severe; in rural areas it is often only serious when there are obstacles such as trees close to the vehicle.

In this chapter, much attention has been devoted to antenna diversity technique aimed at mitigating the deleterious effects of the fading. In this method multiple antennas are used for gathering uncorrelated signals from the environment and by the signals combining reduce the fading effects. The signals combining techniques and the relative effects on the fading are reviewed. Diversity gain is explained as an issue showing the improvement from a diversity system. The diversity gain performance depends on the signals correlation coefficient and the mean power difference in the antenna branches.

The correlation coefficient evaluation techniques using mutual resistance, radiation pattern, signals simulation and measurements are discussed. The performance of space diversity antennas in relation to the propagation environment and antenna placement are computed. The simulation results are applied for characterizing the diversity gain of antennas for correlated fading signals and imbalance branches powers.

Finally, Supelec reverberation chamber is explored for antenna diversity tests. The spatial correlation coefficient is measured for the reverberation chamber and is compared with theoretical results.

proportional to the root mean square signal and inversely proportional to the mean square noise in the  $k^{\text{th}}$  branch.

Scanning and selection combining do not use assumptions (2) and (3), but equal-gain and maximal ratio combining rely on the coherent addition of the signals against the incoherent addition of noise. This means that both equal-gain and maximal ratio combining show a better performance than scanning or selection combining, provided the four assumptions hold.

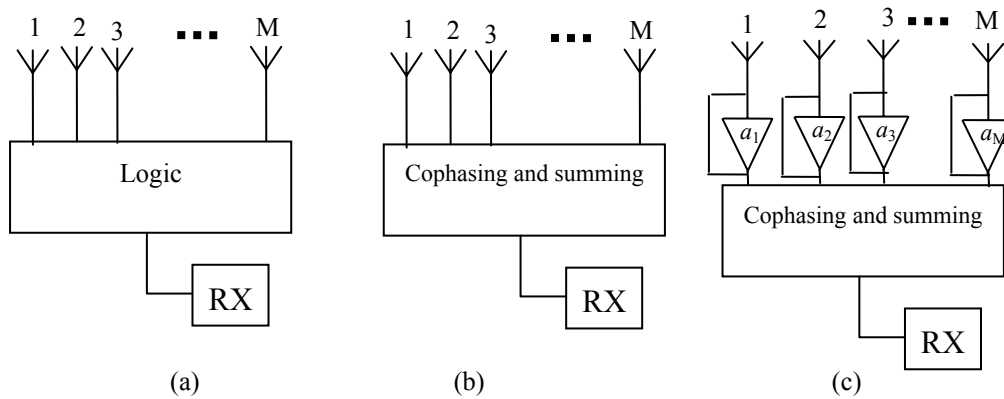


Figure 4-2 Diversity reception systems: (a) selection (b) equal-gain (c) maximum ratio, combining

### 4.3.1 Selection combining

Selection diversity is the simplest of all the diversity combining methods. In an ideal system of this kind the signal with the highest instantaneous CNR is used, so the output CNR is equal to that of the best incoming signal.

$$X_{sc}(t) = \max\{X_1(t), X_2(t), \dots, X_M(t)\} \quad (4-2)$$

In practice it is essential that the switching time of the system is shorter than the signal fading rate. This depends on the bandwidth available in the receiving system. By assuming that the signals in each diversity branch are uncorrelated narrow-band Gaussian processes of equal mean power i.e. their envelopes are Rayleigh distributed, the PDF of the CNR and the CDF (cumulative probability function) i.e. the probability of the CNR that is less than or equal to any specific value,  $\gamma_s$  are depicted in Table 4-1. Where  $\gamma_0$  is defined as the mean carrier power to mean noise power ratio ( $\sigma^2/N$ ).

The PDF, CDF and the mean CNR at the output of combiner for a system with  $M$  diversity branches and selection combining ability are also tabulated in Table 4-1.

diversity is the ability to reduce the number of deep fades in the output signal. In statistical terms, diversity changes the distribution of the output CNR and it no longer has an exponential distribution. This cannot be achieved just by increasing the transmitter power.

To show this effect, the first-order envelope statistics of the signal, i.e. the way the signal behaves as a function of time, Cumulative probability distributions of the composite signal have been calculated for Rayleigh distributed individual branches with equal mean CNR ( $\gamma_0$ ). For two-branch SC, EGC and MRC systems the appropriate cumulative distributions are tabulated in Table 4-1. Figure 4-5 illustrates the CDF of these equations. The CDF of Rayleigh is also illustrated for comparison showing the single branch distribution. It is clear that the diversity curves are much flatter than the single-branch curve, indicating the lower probability of fading.

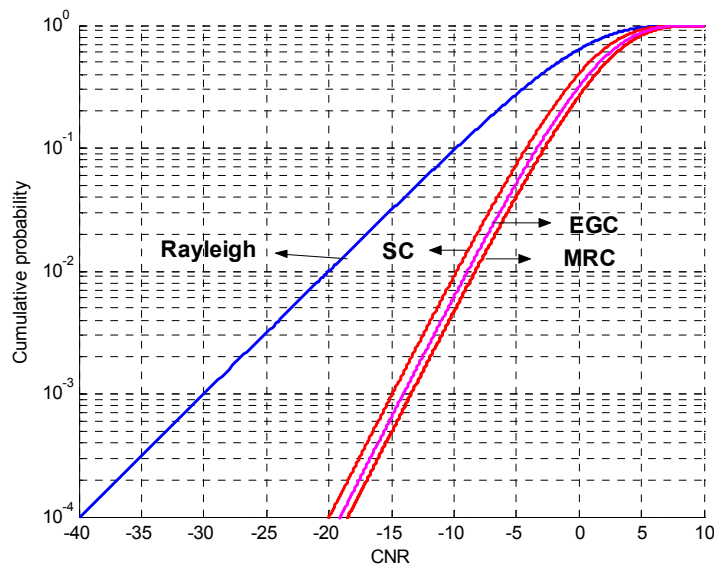


**Figure 4-5 CDF plot of the output CNR for two-branch diversity system for SC, MRC and EGC**

To gain a quantitative measure of the improvement, we note that the predicted reliability for two-branch selection is 99% (0.01 CDF level) in circumstances where a single-branch system would be only about 88% (0.12 CDF level) reliable. This means that the coverage area of the transmitter is far and there are fewer areas in which signal flutter causes problems. A comparable result can be achieved by alternating the CNR improvements in a system with and without diversity application. The diversity gain is defined as the increment in CNR in diversity system by comparison to a system without diversity and for a defined CDF level. For instance in Figure 4-5, the transmitter power would involve an

where  $G$  is the diversity gain in 'dB' for 0.1 level,  $\Delta$  represents the mean signal level difference and  $\rho$  represents the correlation coefficient. The RMS error values are 0.87, 0.74 and 0.79dB for SC, EGC and MRC, respectively. The measurements are performed for 1800MHz band. Figure 4-7 shows the diversity gain versus power difference and correlation coefficient computed based on the equations (4-6a-c).

As shown the gain variations versus correlation and power imbalance are approximated by linear equations but our numerical simulation in section 4.10 gives nonlinear variation of the diversity gain.

#### 4.4.1 Level Crossing Rate and Average Fade Duration

In chapter 2 we have discussed about the first order statistics of the fading signals and it was shown that the fading envelop can be described by Rayleigh PDF. The first order statistics are those for which time (or location) is not a factor and it gives the information such as the overall percentage of time, or the overall percentage of locations, for which the envelopes lies below a specified value. There is no indication of how this time is made up. Level crossing rate (LCR) and average fade duration (AFD) below a specified level are two terms that gives a quantitative description of the rate at which fades of any deep occur and the average duration of the fade below any given depth. This provides a valuable aid for system engineers in selecting bit rates, word length and coding scheme in digital radio systems and allows an assessment of system performance. The manner in which these two parameters are derived is illustrated in Figure 4-8. The LCR at any specified level is defined as the expected rate at which the envelop crosses that level in a positive-going (or negative-going) direction. The average duration  $\tau$ , below any specified level  $R$ , is also illustrated in

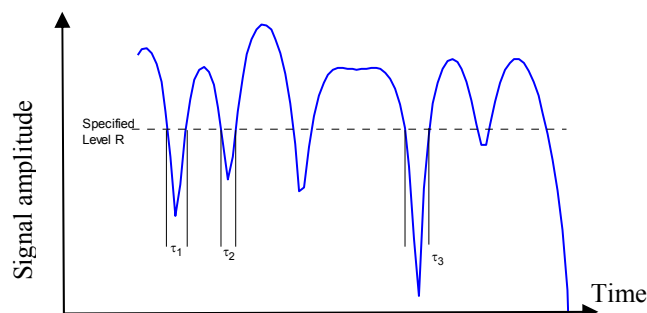


**Figure 4-8 LCR and AFD: LCR is the average number of positive-going crossing per second, AFD is the average of  $\tau_1, \tau_2, \dots, \tau_n$**

### 4.5.2 Correlation coefficient: radiation pattern

The received signal by an antenna in a multipath channel contains the effects of the incident field and the farfield radiation pattern of the antenna. The farfield pattern contains, implicitly, the effects of the mutual impedance between elements.

For a two branch diversity antenna, the complex correlation coefficient between the branches is given by [31]

$$\rho_c = \frac{R_{12}}{\sqrt{MEG_1} \sqrt{MEG_2}} \quad (4-10)$$

where  $MEG$  is the mean effective gain of the antenna for each diversity branch and  $R_{12}$  is the cross-correlation between the two branches [3], [24]. Equation (4-10) can be also expressed as

$$\rho_c = \frac{\int_{\Omega} \left( \frac{XPR}{1+XPR} E_{1\theta} E_{2\theta}^* P_{\theta} + \frac{1}{1+XPR} E_{1\varphi} E_{2\varphi}^* P_{\varphi} \right) d\Omega}{\sqrt{\int_{\Omega} \left( \frac{XPR}{1+XPR} E_{1\theta} E_{1\theta}^* P_{\theta} + \frac{1}{1+XPR} E_{1\varphi} E_{1\varphi}^* P_{\varphi} \right) d\Omega} \sqrt{\int_{\Omega} \left( \frac{XPR}{1+XPR} E_{2\theta} E_{2\theta}^* P_{\theta} + \frac{1}{1+XPR} E_{2\varphi} E_{2\varphi}^* P_{\varphi} \right) d\Omega}} \quad (4-11)$$

where  $\Omega(\theta, \varphi)$  is the spatial angles in steradian,  $E_{1\theta}(\Omega)$ ,  $E_{1\varphi}(\Omega)$ ,  $E_{2\theta}(\Omega)$  and  $E_{2\varphi}(\Omega)$  are the complex envelopes of the  $\theta$  and  $\varphi$  components of the field patterns of the antenna for each port excitation.  $P_{\theta}(\Omega)$  and  $P_{\varphi}(\Omega)$  are the distributions of the AoAs on the antenna in the  $\theta$  and  $\varphi$  polarizations, respectively (have been discussed in chapter 2).  $XPR$  is the cross polarization power ratio (see Table 2-4). The above expression assumes that the incident field powers are normalized to unity and the antenna power gains are normalized to isotropic.

Equation (4-11) is effective for calculating the correlation coefficient from the antenna normalized radiation patterns. This equation contains the mutual effects of the antenna surrounding environment on the correlation coefficient.

Depending on the antenna radiation patterns various types of diversity antennas can be depicted that will offer low correlation coefficient. If the antenna patterns are orthogonal to each other clearly the multiplication of  $E_{1\theta}$  and  $E_{2\theta}^*$  for both  $\theta$  and  $\varphi$  polarizations is zero and the correlation coefficient value is equal to zero this term is known as polarization diversity. If the antennas are spatially separated the correlation coefficient is reduced by the space

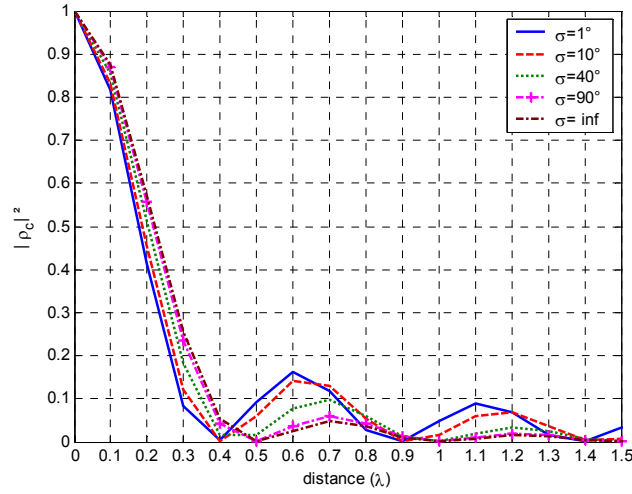


**Figure 4-11 Correlation coefficient between two vertically polarized isotropic antennas versus separation distance  $d(\lambda)$ ; AoAs are given by Taga model for  $m_\theta=0^\circ$  and  $\sigma_\theta$  values**

correlation values. The correlation coefficient for other distribution parameters lies between the two previous curves. For the antenna separations more than  $0.43\lambda$ , the signals correlation for isotropically scatters is less than the other distribution parameters.

Reverberation chamber emulates multipath propagation environment with isotropically scatters. Consequently, the above study reveals that the measured correlation coefficient inside a reverberation chamber is worse than the correlation coefficient in mobile fading environments. Therefore, better antenna diversity performances in the wireless environments with Clarke or Taga model would be desired compared to the reverberation chamber measurements.

Now, we consider that the two antennas in Figure 4-10 are vertically separated in the  $z$ -axis direction. The coordinate translation term in this case is  $\beta d \cos\theta$ , thus (4-16) is expressed as:

$$\rho_c = \frac{1}{2\pi} \int_0^{2\pi} \int_0^\pi [e^{-j\beta d \cos\theta} P_\theta(\theta)] \sin\theta d\theta d\varphi \quad (4-18)$$

The signals correlation coefficient versus vertical separation distance and for the previously defined AoAs is illustrated in Figure 4-12. The correlation coefficient is always near to unity for all separations if the incident field is propagating in the azimuth plane only i.e. *Clarke* model. By increasing the ' $\sigma_\theta$ ' the correlation coefficient is largely reduced for

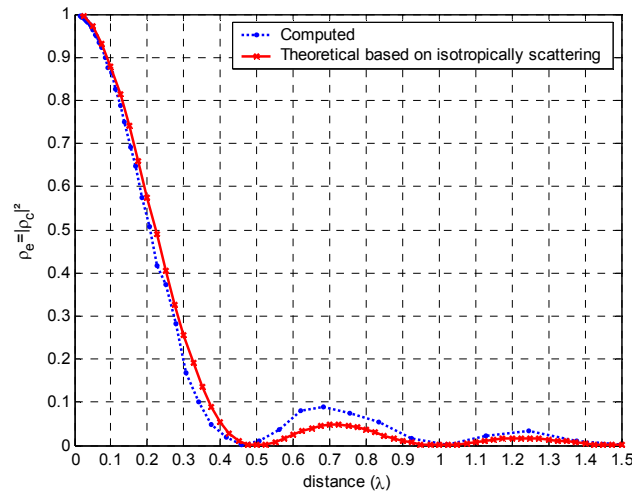


**Figure 4-16 Correlation coefficient between two isotropic radiating antennas versus separation distance. The antennas are exposed to scattering field with isotropic field AoA distribution**

uncorrelated and for  $\beta=0.01$ , 1/50 of the samples are uncorrelated. Therefore for fast simulation it is better to compute the received signals for  $\beta$  value equal to 0.5 instead of small  $\beta$  and large number of samples. This large selected  $\beta$  value is not realistic, because the phase variation rate is directly related to the Doppler spectrum. Appropriate selection of the  $\beta$  is effective for the design of communication systems but it would not change our results for computing the correlation coefficient and diversity gains because these two terms are time independent factors.

The major advantage of the field simulator method is the possibility for simulating the diversity gain, AFD, LCR, in addition to the correlation coefficient.

The developed Matlab code illustrates the auto-correlation of the fading signal and finds the number of uncorrelated samples in the computed signals. The larger the uncorrelated samples the better the estimation of diversity parameters. The question is how many uncorrelated signal samples are sufficient to accurate computation of the correlation coefficient? Figure 4-17 shows the computed correlation coefficient error versus number of uncorrelated signal samples. As shown the correlation coefficient error over less than 100 uncorrelated samples are not stable and have large variations. 100 to 300 samples illustrate an error of less than 0.06 and more samples give an error of less than 0.02. Therefore to have accurate correlation estimation over signal samples more than 100 uncorrelated samples is

#### 4.9 Diversity Gain for Correlated Signals: Numerical Results

We have seen that different separation distance between the antennas offer various correlation coefficients from unity to zero for  $d=0\sim 0.4\lambda$  (see Figure 4-15). Therefore it is interesting to express the diversity gain versus the correlation coefficient based upon the CDF of the simulated signals. Figure 4-22 and Figure 4-23 show the computed diversity

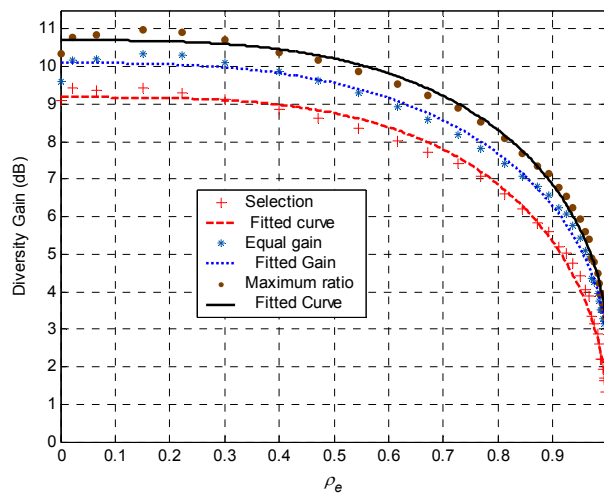


Figure 4-22 Diversity gain (dB) versus correlation coefficient for  $\alpha=0.01$  and for selection, equal gain and maximum ratio combining. The best fitted curve is also illustrated for each case of combining

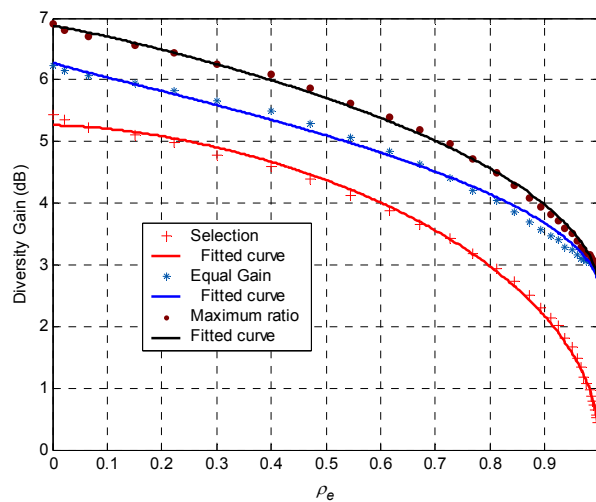
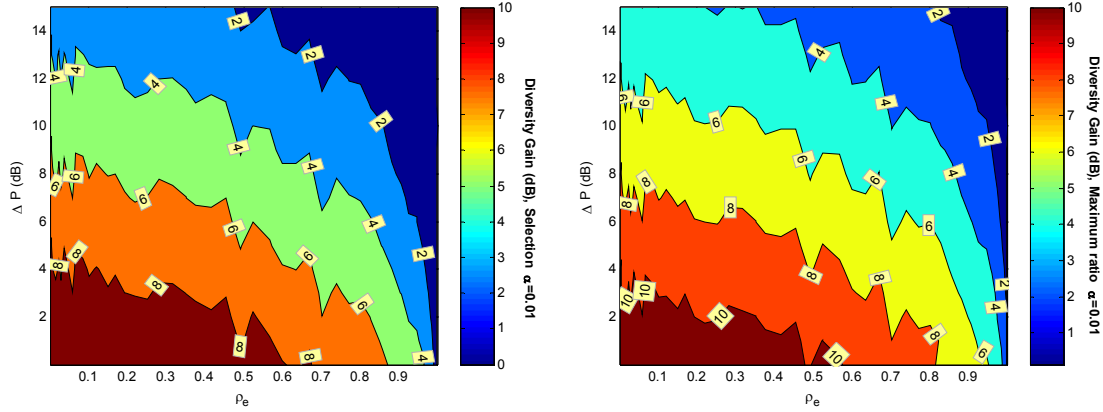


Figure 4-23 Diversity gain (dB) versus correlation coefficient for  $\alpha=0.1$  and for selection, equal gain and maximum ratio combining. The best fitted curve is also illustrated for each case of combining.

around 8dB. The gain for MRC for  $\Delta P < 3\text{dB}$  and  $\rho_e < 0.6$  has the maximum around 10dB. The computed gain variation results are nonlinear and are different from the values given in Figure 4-7.



**Figure 4-26 Diversity gain against correlation coefficient and power imbalance for  $\alpha=0.01$ ; (Left) SC and (Right) MRC**

#### 4.11 Diversity Evaluation from Measured Signals

The correlation coefficient and diversity gains can be evaluated from the measured complex signals, signals voltage or signals power as explained in section 4.5.3.

The received signal in real environments contains the effect of the propagation loss due to different distances from the transmitter and is known as *slow-fading*. During a dynamic measurement of the signals, as the distance and obstacles between the transmitter and receiver vary, the overall strength of all the multipath components will experience similar variations simply due to the changing environment. This long-term, or slow-fading, is not a function of multipath and should be ignored in the diversity computations. The *demeaning* of the data before calculation of the correlation is important to remove the slow-fades effects. This can be accomplished by extracting the local mean of the measured data before performing the diversity computations. By local mean, it means a relatively long-term moving average of the observed envelopes.

By assuming that the slow-fading is a multiplication factor of the observed envelopes and letting  $r(t)$  be the observed envelope,  $\hat{m}(t)$  the local mean which contains the slow-fading information and  $r_o(t)$  the fast-fading envelope, these terms can be related as

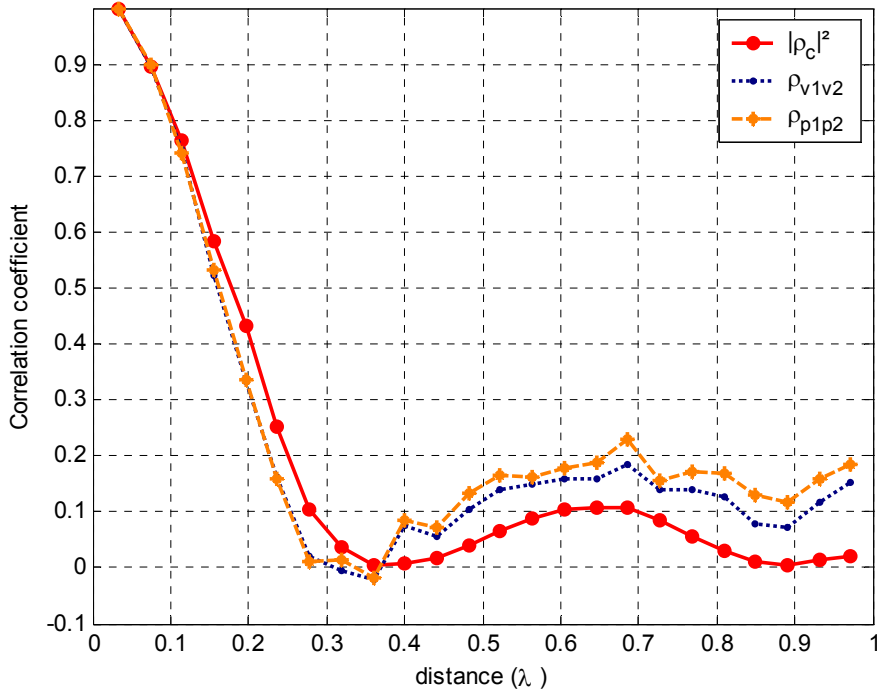


**Figure 4-28 correlation coefficient between spatial points measured inside reverberation chamber; square envelop of the complex correlation, correlation between signals voltage and correlation between signals power are illustrated**

evaluation of antennas, the measurements can be performed in two or more different locations with displacement of about  $0.4\lambda$  to each other.

To compare the above measurement results with the theoretical values the signals correlation coefficient is computed from the radiation patterns using equation (4-13). An isotropically scatters and unpolarized case ( $XPR=1$ ) environment is supposed and the radiation pattern of vertically oriented dipole antenna is used given by

$$E_{\theta}^1 = A \left[ \frac{\cos\left(\frac{\beta l}{2} \cos \theta\right) - \cos\left(\frac{\beta l}{2}\right)}{\sin \theta} \right] \quad (4-22a)$$

$$E_{\theta}^2 = E_{\theta}^1 \exp(-j\beta d \cos \varphi \sin \theta) \quad (4-22b)$$

where  $\beta$  is the wave number and  $l$  is the dipole antenna length.  $E^1$  is the antenna patterns for z-axis oriented dipole in the center of the computational domain and  $E^2$  is the pattern of

imbalanced and the branch signals are correlated the system performance is mitigated. The diversity gain variation curves for the present condition are computed.

Diversity performance can be evaluated by direct measurements in multipath fading channels. The measured signals must be processed to eliminate the slow fading effects; the data demeaning is a technique in this approach. Reverberation chamber based measurement does not require the data demeaning due to the fact that the distance between the transmitting antenna and the receiving antenna is constant.

Signal sounding in Supelec reverberation chamber is conducted to evaluate the correlation between spatial locations in the chamber. An especial setup is used to measure the correlation coefficient variations. Envelop, voltage and power correlations versus distance are measured. The measured decorrelation distance inside the reverberation chamber is  $0.4\lambda$ ; this specifies the effective spatial displacement for gathering large number of uncorrelated signal samples. LCR and AFD curves are measured in the MSRC and are compared with the theoretical curves given for mobile multipath channels. Good accordance is resulted.

It is also shown that the patterns can have very similar shapes and still be uncorrelated if the patterns phases are different.

The simulations are followed by laboratory measurements carried out in Supelec reverberation chamber. The measurements are performed at 2450MHz with two standard (half-wave) dipole antennas; the signals correlation coefficient is precisely measured with high resolution of the antenna distances, has not been performed before [67]. The selected high frequency and the large chamber size increase the measurement accuracy.

Diversity gain for SC and MRC versus dipoles separations are computed from the measured signals. Effective diversity gain which represents the gain over a single antenna and includes the influence of correlation coefficient and mean effective gain is measured. The mean received power degradation at the coupled antennas is measured and is compared with the modeled antenna radiation efficiency.

### 5.2.1 Signals Correlation coefficient: radiation pattern

The signals correlation coefficient between two antenna patterns in an isotropically scattering field environment and unpolarized case ( XPR=1 ) is given by equation (4-13). This model of the field scatters corresponds to the reverberation chamber multipath or equally indoor environment where there are many nearby scatters [70]. If the antennas are vertically polarized, as is the case in parallel side-by-side and z-oriented dipoles ( $E_{1\phi}=E_{2\phi}=0$ ), equation (4-13) is simplified to

$$\rho_c = \frac{1}{4\pi} \int_{\Omega} E_{1\theta}(\Omega) \cdot E_{2\theta}^*(\Omega) d\Omega = \frac{1}{4\pi} \int_{\Omega} |C(\Omega)| e^{j\Psi(\Omega)} d\Omega \quad (5-1)$$

Equation (5.1) is expressed as a function of the pattern-coupling magnitude and pattern-coupling phase factors,  $|C(\Omega)|$  and  $\Psi(\Omega)$ , respectively. The signals envelop correlation coefficient is related to the complex correlation (5-1) by the equation (4-7).

The correlation coefficient between two identical patterns which are circularly symmetric and horizontally separated with distance 'd' is given by the zero order Bessel function  $J_0(\beta d)$ , where  $\beta$  is the wave number. This is so called Clarke function and shows the space diversity effects [51].

The correlation coefficient between two half-wave dipoles Figure 5-2, which are parallel, z-oriented and horizontally separated with distance d, can be computed from the dipole

The signals correlation coefficient is computed from the modeled complex pattern using (5-1) and (4-7). The envelop correlation coefficient against separation distance is plotted in Figure 5-6. As shown, small envelop correlation is obtained even for small antenna apart, for instance for  $d=0.05\lambda$  gives  $\rho_e=0.35$  and for  $d=0.1\lambda$  gives  $\rho_e=0.1$ . Therefore, the envelop correlation for small antenna separations is considerably reduced compared to the theoretical value.

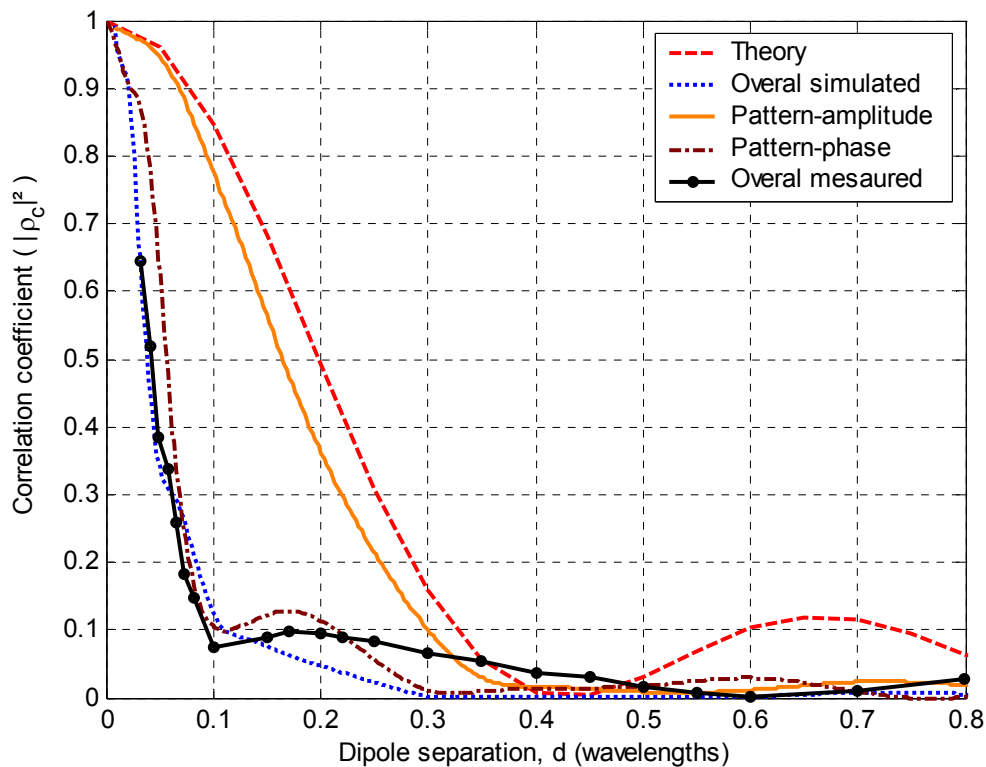


**Figure 5-6 Correlation coefficient as a function of antenna spacing (wavelengths), simulated and measured inside an isotropically scattered field environment. (---) Theory calculated; (...) overall simulated; (—) simulated using pattern-amplitude diversity effects; (-·-·) simulated using pattern-phase diversity effects; (-o-) overall measured inside mode stirred reverberation chamber**

Figure 5-5a illustrates the farfield pattern for  $d=0.1\lambda$ , the two patterns are almost similar and the impact of the space diversity is too small to reduce the correlation coefficient to 0.1. Therefore, we could anticipate that an effective diversity term is generated in addition to the two well-known space and pattern diversities and the signals correlation is greatly reduced.

For the selected diversity structure the antennas are both vertically oriented and the radiation pattern for all separation distances are always vertically polarized i.e. there is not

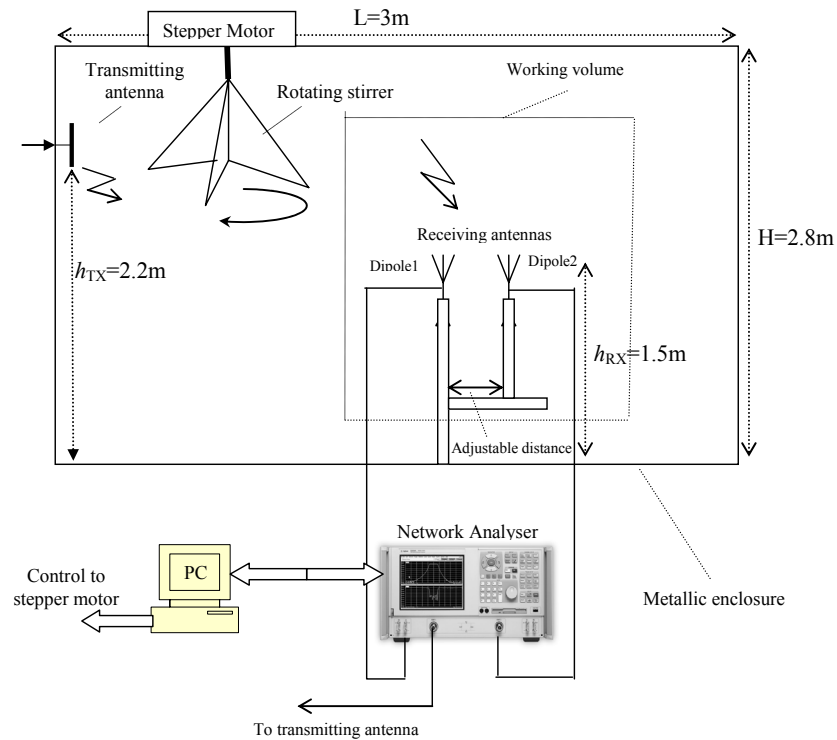


**Figure 5-9 Reverberation chamber measurement setup for two port signal acquisition**

due to time variable multipath propagation generated by the rotating stirrer. The signals amplitude variations are detected by the receiver system of the network analyzer and the signals are sampled and stored in the internal buffer of the network analyzer. The internal buffer can record up to 1601 samples of the signals. Using the single trace mode the signal samples are recorded and then stored in an external disk for offline processing. The statistical properties of the received signals for one revolution of the stirrer are complex Gaussian and the cross polarization ratio of the scattered field is unity. The measurement inside the chamber is repeatable with periodically rotation of the stirrer. The above approach offers a reasonable measurement time for signals acquisition i.e. the measurement time for single frequency with two receiving antennas takes 100sec.

In the measurement procedure we have avoided the use of frequency stirring used in [67], [68]. This is because, when the frequency is changed the normalized distance between the antennas is corrupted and this gives smaller accuracy for small separation distance measurements. Furthermore, the frequency stirring makes changes in the antenna port

is reduced by the absorption and mismatch effects [67], [73]. To include this effect in diversity gain, we extract the gain in relation to the CDF plot of a single antenna measured at the identical propagation channels (effective diversity gain). Figure 5-13 illustrates the measured effective diversity gain versus dipoles separation. As shown, the gain is smoothly reduced (about 1dB) within  $0.5\lambda$  and  $0.15\lambda$  apart; in smaller distances the gain is rapidly dropped. This is a good result showing the limit of coupled antenna spacing for effective diversity application. It can also be concluded that, a small correlation coefficient is not the sufficient condition for optimum diversity gain performance i.e. the efficiency of the antennas would affect the effective gain of the diversity antenna configurations.

Referring to Figure 5-4 the mutual power coupling between the parallel dipole antennas for  $d=0.15\lambda$  is -5dB. Therefore, a power coupling of -5dB can be tolerated between coupled antennas without significant loss of the effective diversity gain.

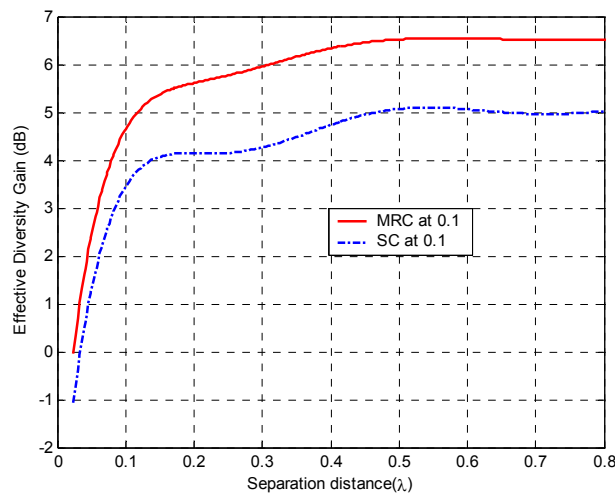


**Figure 5-13 Measured effective diversity gain (dB) versus dipole separation ( $\lambda$ ) for selection combining (SC) and maximum ratio combining (MRC) at 0.1 CDF level**

#### 5.2.4 Antenna efficiency

In this section, we compare the modeled antenna radiation efficiency with the measured mean powers inside reverberation chamber. The radiation efficiency is most conventionally calculated in transmit mode and it is the same on reception, due to reciprocity. In the coupled antennas the radiation efficiency is degraded by absorption in neighboring antenna or by impedance mismatch at antenna terminals. The antenna efficiency for various dipole separations is calculated using TLM method by exciting one antenna and  $50\Omega$  terminating of

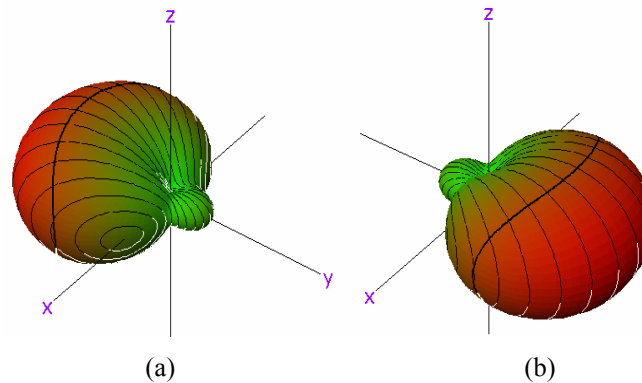


**Figure 5-17 Simulated radiation pattern of dipole diversity system for  $d=0.15\lambda$ , and a)  $Z_1=\infty, Z_2=0$   
b)  $Z_1=0, Z_2=\infty$**

incident fields. The major problem is occurred for a smaller distance is the impedance matching of the active antenna that is changed by the mutual effects of the parasite elements. This results to a reduced radiation efficiency and therefore smaller mean effective gain. For example, the radiation efficiency of the active antenna is reduced about 1dB for  $d=0.15\lambda$ , 1.5dB for  $d=0.1\lambda$  and 5.5dB for  $d=0.05\lambda$ . The radiation efficiency degradation for the proposed configuration that uses non resistive loads is reduced by the mismatching effects of the antennas. If a resistive load is used the radiation efficiency is more reduced due to field absorption by the resistive impedance.

A compact diversity configuration can be developed using one active radiating antenna and using only one parasitic element. Mattheijssen [72] has presented a diversity configuration containing one active radiating dipole antenna and one parasite dipole element. The load impedance of the parasite is switchable between two different impedances ( $Z_1$  and  $Z_1'$ ). The optimized loads are  $Z_1=-j20\Omega$  and  $Z_1'=-j100\Omega$  and the antennas distance is  $d=0.1\lambda$ . By these assumptions, the radiation patterns are computed for both cases and are illustrated in Figure 5-18. As shown two patterns are small overlapped and the signals envelop correlation receiving through these two patterns is 0.39 [72]. The analysis conducted by Mattheijssen suppose Clarke model for AoAs and uses only the radiation pattern amplitude of the antennas in the azimuth plane. Based on our detailed analysis the envelop correlation coefficient is 0.22 for Clarke AoA model and considering complex pattern. If an isotropically scattering environments is considered the correlation is reduced to 0.15. Equal amount of correlation is depicted by considering the field amplitude only and Clarke field

are obtained using wire model available by the package. The dimensions of the grids around the wire model of the helical antennas are manually small selected (0.5mm in both x and y directions and 0.25mm in z direction), therefore the helical antenna would be precisely constructed after the model discretising. The total number of realized cells after meshing was 93104 and the allocated memory was 15M. The computation time using normal P4 with 512M RAM takes 12 minutes for two ports simulations.

The return loss in diversity branches and the mutual coupling of the constructed prototype are experimentally measured using a calibrated network analyzer. The return loss measurements are performed in a condition in which one antenna is connected to the network and the next one is terminated to  $50\Omega$  load impedance. The measurement results are different from single port antenna measurement because the induced current on the non-excited antenna would change the current distributions along the excited element; therefore the port impedance would be modified.

It is notable that the commercial helical antenna uses one helical turn around a metallic core at the beginning of the helix for impedance matching, the plastic material are used as the helical antenna core and the antenna is coated with plastic material. In the simulations procedure we have not considered these options. The measured return-loss of the Sagem helical antenna illustrates two resonance frequencies on 1010MHz and 1970MHz. These frequencies are out of the GSM and DCS bands. To apply the antennas in the mobile frequency bands we have coated the two antennas with additional isotherm plastic materials therefore the two resonance frequencies are moved down to GSM/DCS bands.

The measured and simulated return loss for the antenna ports are given in Figure 5-21. The simulated return loss for the second resonance frequency is small different from the measurements. The impedance matching of the simulated model is worse than the measurements, this issue results to smaller radiation efficiency of the simulated pattern.

The mutual power coupling ( $S_{21}$ ) between antenna ports is measured when one antenna is transmitting and the other antenna is receiving. As shown in section 5.2 the mutual power coupling has negative effects on the radiation efficiency but illustrate positive effects on the signals correlation coefficient for diversity configurations. The measured and the simulated mutual coupling versus frequency are illustrated in Figure 5-21. The antenna prototype is symmetric, therefore similar results are observed for both antennas.

#### 5.4.4 Signals correlation coefficient: mutual impedance

In section 4.5.1 it has been shown that the signals correlation coefficient can be approximated by the normalized mutual resistance. To evaluate the mutual resistance the complex scattering parameters of the antenna array are measured then, the conversion of S-parameters to Z-parameters is performed. The approach is different from the direct measurement of the Z-parameters using the network analyzer in the Smith chart operating mode. This is because, the measured mutual impedance contains the effects of the self-impedance that should be removed from the measurements.

The measured port impedance for 938MHz is  $Z_{11}=47.5-j 2.6$  and the mutual impedance is  $37.6+ j4.1$ ; this gives the normalized mutual resistance  $r_{12}=0.79$  and consequently envelop correlation of  $\rho_e=0.62$ . For 1830MHz the port impedance is  $Z_{11}=41.7 +j14.7$  and the mutual impedance is  $19 +j12.8$ ; this results the normalized resistance  $r_{12}=0.45$  and consequently  $\rho_e=0.2$ .

The signals correlation coefficient is evaluated using radiation pattern and random field measurement in the following sections. It has been shown that the given correlation coefficient is considerably different from the mutual impedance approach.

#### 5.4.5 Signals correlation coefficient for GSM band: pattern approach

Signals correlation coefficient is computed by the direct method (equation (4-11)) and applying the antenna patterns and the field AoA models. The AoA models are given in Table 2-3 and the cross polarization ratio of the scattered field is supposed to be unity (XPR=1) for all models.

For the GSM band the signals correlation coefficient is computed using the simulated and the measured antenna patterns. Table 5-1 and Table 5-2 show the complex correlation coefficient and the envelop correlation coefficient for various field scattering models. The AoAs are specified with  $M_0$  corresponds to the model with isotropically scatters;  $M_1$  is related to Clarke model with uniform scatters in the azimuth plane only;  $M_{2-1}$  and  $M_{2-2}$  are supposed Gaussian distribution in the elevation and uniform in the azimuth (index 1 and 2 are related to Taga model parameters);  $M_3$  considers double-exponential distribution in the elevation and uniform scatters in the azimuth (the double exponential parameters are given in Table 2-3, we have selected the average of all environment (see Table 2-2) to construct the double exponential model. The last model  $M_4$  corresponds to the elliptical model for the

MRC, respectively. The lower probability level gains illustrate about 1dB discrepancy compared to the case with 2000 signal samples and  $\beta=0.5$ .

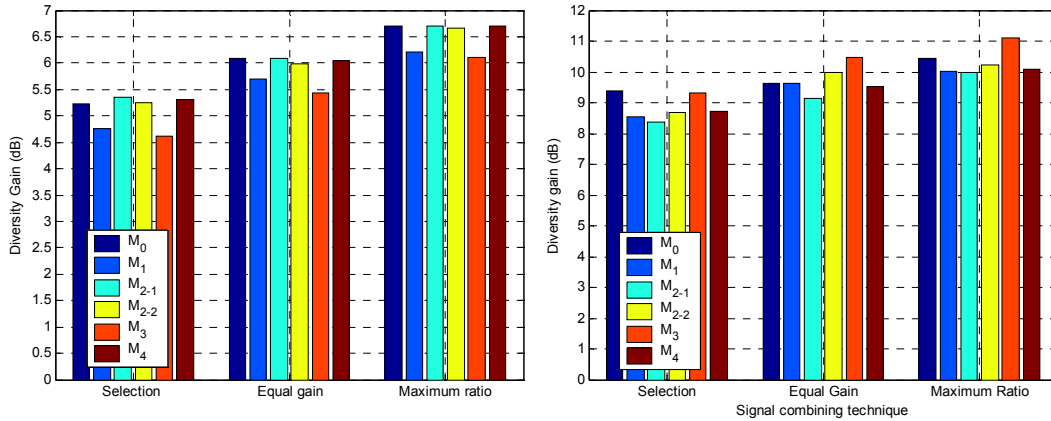


Figure 5-28 Diversity gain (dB) for different AoAs and combining techniques based on the measured pattern in the GSM band Left)  $\alpha=0.1$  Right)  $\alpha=0.01$

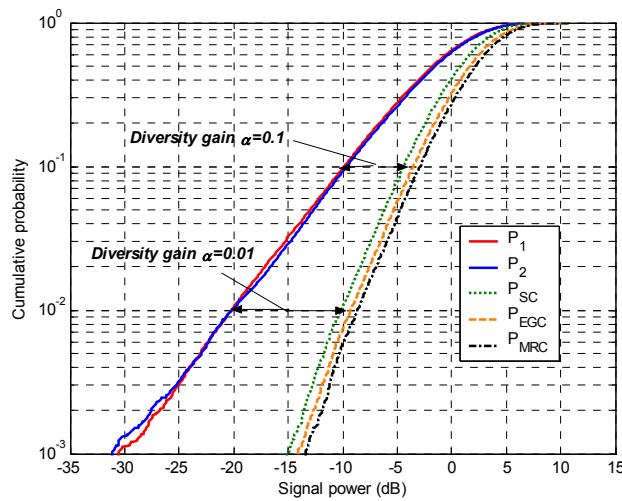
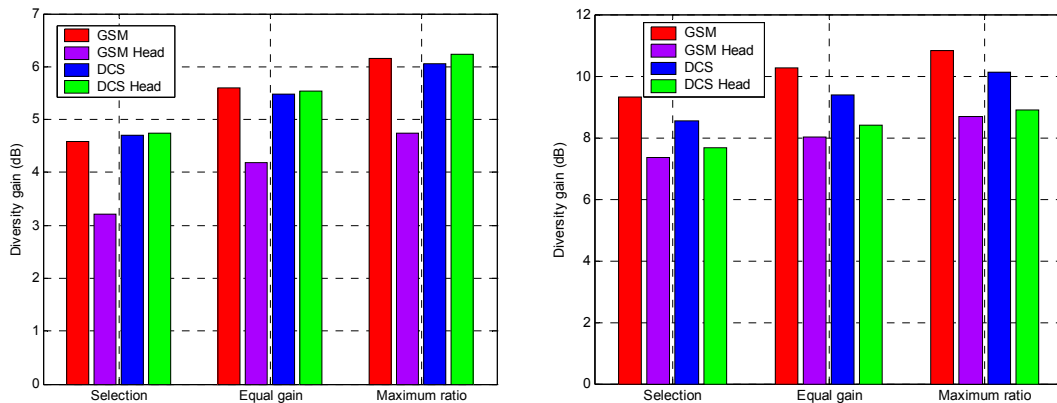


Figure 5-29 CDF of the modeled signals in the diversity branches and after combining: SC, EGC and MRC

Figure 5-30 shows the LCR of the computed signals and the signals after combining. The theoretical LCR is also illustrated for the comparison. The simulated curve is fairly in good accordance with the theoretical one.



**Figure 5-39 Measured diversity gains for SC, EGC and MRC with and without phantom human head for the GSM and DCS frequency bands (Left)  $\alpha=0.1$  (Right)  $\alpha=0.01$**

The mean signal power in the antenna branches at the presence of the phantom human head is reduced 11.2dB and 8.2dB for the GSM and the DCS bands respectively. These values are related to the absorbed powers by the human head and also the impedance mismatching of the antennas.

#### 5.4.10 Correlation coefficient and diversity techniques

The signals correlation coefficient based on Clarke function for two spatially separated antennas with distance  $d$  is given by  $J_0(\beta d)$  where  $J_0(\cdot)$  is the zero order Bessel function and  $\beta$  is the wave number. The correlation coefficient based on Clarke function for the GSM band ( $d=\lambda/8$ ) is 0.72 and for the DCS band ( $d=\lambda/4$ ) is 0.22. The computed and the measured correlation coefficient are significantly smaller than these values. This can be explained by the fact that, in the Clarke function the radiation patterns are similar and the space diversity is the main diversity technique that reduces the correlation coefficient.

We have shown that the radiation patterns of the antennas are affected by the handset box and the mutual coupling; therefore, the radiation patterns are not symmetric (see Figure 5-25 and Figure 5-31). A composite form of diversity techniques are generating in addition to the well-known space diversity. Different diversity techniques are distinguished as space, polarization and pattern (amplitude and phase). The correlation coefficient, for the GSM band, based on the radiation pattern amplitude only is 0.62. The correlation coefficient based on the radiation pattern-phase (with removed space diversity effect) is 0.71.

### 6.2.2 Theoretical Analysis

Current and electrical field are two possible coupling sources in printed antennas. For the proposed circular patch two orthogonal  $TM_{11}$  modes are excited with two  $90^\circ$  rotated feeds. The  $TM_{11}$  mode currents on the patch are given as [79]:

$$J_\varphi = \frac{j}{\omega\mu\rho} E_0 J_1\left(\frac{X'_{11}\rho}{a}\right) \sin\varphi \quad (6-1)$$

$$J_\rho = \frac{-jk}{\omega\mu} E_0 J_1'\left(\frac{X'_{11}\rho}{a}\right) \cos\varphi \quad (6-2)$$

where  $J_l(\cdot)$  is first order Bessel function,  $\rho$  and  $\varphi$  are cylindrical coordinate system parameters,  $a$  is the patch radius and  $X'_{11}=1.84$ . From these equations it is clear, from the sin/cos dependences, that the current induced at port  $P_2$ , when port  $P_1$  is excited, is orthogonal to the current at port  $P_2$  when this port is excited. Hence, the current excited by one of the two ports is not exciting the other port. As results there is no current coupling between the orthogonal modes.

The electrical field inside the dielectric layer for  $TM_{11}$  mode is [79]

$$E_z = E_0 J_1\left(\frac{X'_{11}\rho}{a}\right) \cos\varphi \quad (6-3)$$

As in the case of currents, there is no electric field coupling between the orthogonal  $TM_{11}$  modes, when the feeding ports are shifted by  $90^\circ$ . The above analysis on the current and electrical field couplings explains a high isolation between the two antenna ports.

### 6.2.3 Antenna simulation and measurements

The circular patch with two feeding ports is simulated with IE3D method of moment (MOM) commercial code. The antenna is also modeled with TLM code commercially available with Flomerics. Figure 6-2 shows the measured and the simulated return loss and coupling curves for  $P_1$ . As shown, the antenna provides a good return loss -16dB and a good isolation, better than 30dB, between the two ports at 2450MHz. The measured bandwidth is almost 40MHz for a return loss less than -10dB. The 30dB isolation makes the antenna appropriate for polarization diversity and also allows to use the antenna without duplexer for transmit and receive in which the signal paths are well separated.

through the measurements. Our study reveals that the pattern diversity based upon the monopole active element is not a good choice for WLANs that needs larger bandwidth and also good impedance matching.

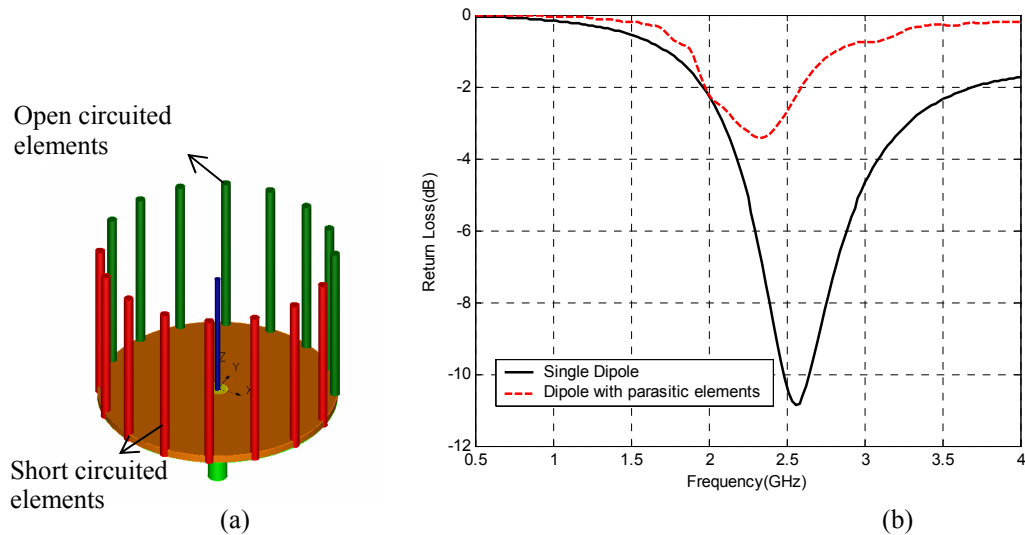


**Figure 6-20 (a) The modeled pattern diversity antenna on a finite ground plane with 16-parasitic elements. (b) Return loss versus frequency for single monopole on the ground plane and after installing the parasitic elements**

Considering the above approach we have replaced the simple monopole antenna by a meander shaped prototype. The meander line technology offers larger bandwidth and also smaller antenna size. The antenna design is optimized for WLAN applications (at 2450MHz) by good impedance matching at the antenna port and sufficient impedance bandwidth. Two uncorrelated patterns are generated by selecting an appropriate configuration of the parasitic rods and connecting or disconnecting the rods to the ground plane. The AoA for indoor scattering channels is about isotropically distributed; therefore to have good signal reception all spatial angles should be covered by the antenna patterns.

### 6.3.2 Main radiator antenna design

Figure 6-21 shows different meanderline and dual-meanderline shaped monopole antennas on a circular ground plane. The configuration (a) is a single meandered wire antenna (b) is a dual meander shaped and (c) is a dual meander shape with an open ended configuration. The horizontal and the vertical lengths of the meander antennas are equally selected. Six

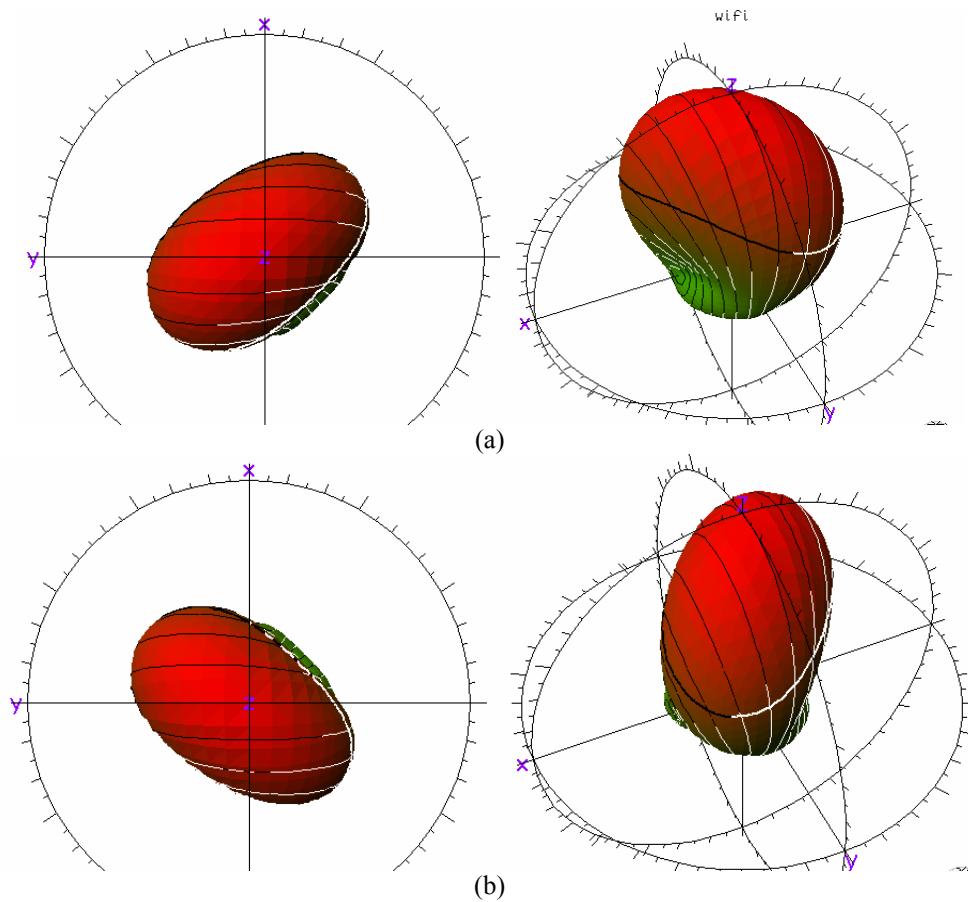


**Figure 6-38 Simulated 3-D pattern of the NPS antenna (Top view and isometric view) (a)  $P_1$  (b)  $P_2$  excitations**

while the other port is connected to a matching load. Figure 6-39 shows the measured 3-D isometric patterns of the NPS antenna for each port excitation, the top view of the patterns are also compared.

#### 6.4.5 Diversity antenna parameters evaluation

The first approach for computing the signals correlation coefficient is based on the normalized mutual impedance (see section 4.5.1). In section 5.4.4, we have shown that the impedance approach for mobile phone diversity antenna is not always good approximation for signals correlation coefficient.

In the present study, the impedance characteristics are evaluated from the complex scattering parameters by converting to Z-parameters. The measured self and mutual impedances versus frequency are given in Figure 6-40. The self impedance for 2450MHz is

illustrate too small signals correlation coefficient and consequently good diversity gain. The measured MEG of the antennas is 1.5dB better than a standard half-wave dipole antenna. The antennas are appropriate for installing on the access point of the WiFi systems.